ACS APPLIED MATERIALS & INTERFACES

Research Article

www.acsami.org

Elucidating the Intercalation Pseudocapacitance Mechanism of MoS_2–Carbon Monolayer Interoverlapped Superstructure: Toward High-Performance Sodium-Ion-Based Hybrid Supercapacitor

Rutao Wang,[†] Shijie Wang,[†] Xiang Peng,[‡] Yabin Zhang,[†] Dongdong Jin,[†] Paul K. Chu,[‡] and Li Zhang*[,†]

[†]Department of Mechanical and Automation Engineering, The Chinese University of Hong Kong, Shatin NT, Hong Kong SAR 999077, P. R. China

[‡]Department of Physics and Materials Science, City University of Hong Kong, Tat Chee Avenue, Kowloon, Hong Kong SAR 999077, P. R. China

Supporting Information

ABSTRACT: Two-dimensional (2D) layered materials have shown great promise for electrochemical energy storage applications. However, they are usually limited by the sluggish kinetics and poor cycling stability. Interface modification on 2D layered materials provides an effective way for increasing the active sites, improving the electronic conductivity, and enhancing the structure stability so that it can potentially solve the major issues on fabricating energy storage devices with high performance. Herein, we synthesize a novel MoS_2–carbon (MoS_2–C) monolayer interoverlapped superstructure via a facile interface-modification route. This interlayer overlapped structure is demonstrated to have a wide sodium-ion intercalation/deintercalation voltage range of 0.4–3.0 V and the typical pseudocapacitive characteristics in fast kinetics, high reversibility, and robust structural stability, thus displaying a large reversible capacity, a high rate capability, and an improved cyclability. A full cell of sodium-ion hybrid supercapacitor based on this MoS_2–C hybrid architecture can operate up to 3.8 V and deliver a high energy density of 111.4 Wh kg^{-1} and a high power density exceeding 12 000 W kg^{-1}. Furthermore, a long cycle life of 10 000 cycles with over 77.3% of capacitance retention can be achieved.

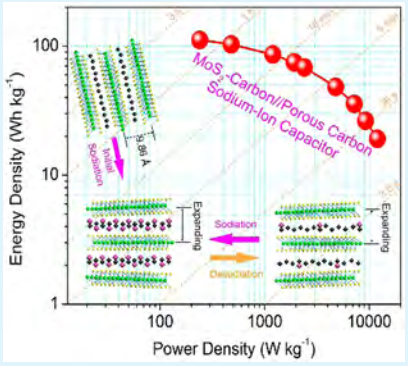

KEYWORDS: *MoS_2, nanocomposite, intercalation pseudocapacitance, sodium-ion storage, supercapacitor*

INTRODUCTION

Supercapacitors (SCs) are electrochemical energy storage devices that store and release ions on a porous electrode with high surface area.[1,2] SCs can operate on an extremely high-power rate about 10 times higher than that of batteries and have a long life span of over a million cycles. However, SCs store a relatively lower energy density than that of lithium-ion batteries, which is a major limitation for their practical applications.[3,4] For example, commercially available SCs, which are mainly composed of two activated carbon electrodes in a symmetric configuration, only deliver a limited energy density (less than 10 Wh kg^{-1}), even operating at a high potential of 2.7 V or more in organic electrolytes. In the past decade, a lot of studies have thus paid more attention to boost the energy density of SCs without downsizing the high-rate capability and the cycling stability.[5−8] One effective method to boost the energy density of SCs is to build a hybrid configuration in which two distinct electrodes with different charge storage mechanisms are paired.[2] This hybrid design, namely, ion capacitor, is usually composed of a battery-type or pseudocapacitor-type electrode and a double-layer capacitive carbon electrode in organic electrolytes, which can deliver higher energy density than conventional SCs.[4,9,10]

Ion capacitors based on lithium salt have been well progressed based on numerous host materials such as graphite,[11] hard carbon,[12] $Li_4Ti_5O_{12}$,[13] MXenes,[14] and Nb_2O_5.[15,16] However, the increasing scarcity of availability of Li leads to the development of more economically favorable sodium-ion capacitors (SICs).[17,18] The abundance of sodium in Earth is about 3 orders of magnitude higher than lithium, rendering its overall resources practically unlimited.[18] Unfortunately, only a few anode materials are available for Na^+ storage owing to the large size of Na^+ ions (radius of >1.02 Å), thus presenting a major challenge for SICs.[17,19] Graphite is considered as an ideal anode material for LICs, which however cannot be well intercalated by Na^+ ions.[18] Recently, hard carbon with the highly electrochemical capacities up to 200 mAh g^{-1} was considered as the most commonly used anode materials in Na-ion based energy storage devices, but showing the relatively poor rate performance caused by Na-ions diffusion in hard carbon along channels and cavities with an irregular geometry.[19,20] Other anode materials, including those

Received: July 6, 2017
Accepted: September 7, 2017
Published: September 7, 2017

DOI: 10.1021/acsami.7b09813
ACS Appl. Mater. Interfaces 2017, 9, 32745−32755

that can largely store Na ions through alloying and conversion mechanisms, have been widely explored.[21−25] The main issues for these materials are the limited cycling stability and poor kinetics owing to the volume expansion and undesirable side reactions.[17,18] Therefore, there is an urgent need to explore novel anode materials with large reversible capacity, fast kinetics, and long cyclability to achieve high-performance SICs.

MoS_2 with its two-dimensional (2D) atomic layered structure, by contrast, is recently considered to be a proper choice for sodium based energy storage devices.[26−36] This is mainly because its 2D layered structure can provide large surface area and permeable slit-shaped channels to facilitate ion insertion/extraction within an individual monolayer.[8,28,29] However, bare MoS_2 usually shows unsatisfactory electrochemical performance in sodium-ion charge storage because of poor conductivity, cracking structure, unstable solid−electrolyte interphase (SEI) layer, and parasitic reactions related to electrolyte decomposition.[8,29] Recent advances show that atomic interface modification of 2D layered materials is able to improve sodium ion charge storage properties through increase of the intrinsic conductivity, structural stability, and intercalation sites.[28,30−34] Therefore, atomic interface modification on MoS_2 may be a promising method to fabricate robust sodium host anodes with high structural stability, long cycle life, and fast kinetics for sodium-ion based energy storage devices. As we know, individual MoS_2 or MoS_2 based composites have rarely been employed as the anode materials for SICs.

In this work, we report that a novel MoS_2−carbon monolayer interoverlapped superstructure via a facile interlayer-modification route features both the pseudocapacitive and extended Na-ion storage properties, which is confirmed by various analyses including electrochemical kinetics and ex situ structural and spectral technologies. Such superior Na-ion storage anode material enables SICs with high energy/power densities and long lifespan. A new type of SIC using this pseudocapacitive MoS_2−carbon monolayer interoverlapped superstructure as the anode shows excellent electrochemical properties in energy, power, and cycling stability, holding great promise for application in various energy storage devices.

EXPERIMENTAL SECTION

Preparation of MoS_2−Carbon Monolayer Interoverlapped Superstructure. MoS_2−carbon (MoS_2−C) monolayer interoverlapped superstructure was prepared using a hydrothermal method. Specifically, 0.3 g of $Na_2MoO_4{\cdot}2H_2O$ (AR, 99.0%) and 0.6 g of thiourea (AR, 99.0%) were dissolved into 20 mL of ultrapure water. After that, an amount of 1.2 mL of poly(diallyldimethylammonium chloride) solution (PDDA, Mw 100 000−200 000, 20 wt %) was added into the solution. After being stirred for 10 min, the mixture was poured into a Teflon-lined stainless steel autoclave (30 mL). And then the autoclave was put in an air-dry oven and heated at 200 °C for 24 h. After that, the mixture in autoclave was centrifuged at 5000 rpm for 10 min and washed with ultrapure water for several times to obtain a black precipitation. The obtained black precipitation containing MoS_2−PDDA composite was dried in a freezing dryer for 24 h. The as-prepared MoS_2−PDDA precursor was further heated at 800 °C for 2 h in an Ar atmosphere with a heating rate of 1 °C min^{-1} to obtain the MoS_2−C sample. For comparison, bare MoS_2 sample was prepared through a similar route but without adding PDDA.

Materials Characterization. The structure, composition, and surface morphology of the samples were investigated by powder X-ray diffraction (XRD, Rigaku D/Max-2400, Japan) using Cu Kα radiation, field emission scanning electron microscopy (FESEM, JSM 7800F, JEOL, Japan), transmission electron microscopy (TEM, TECNAI TF20, FEI), and micro-Raman spectroscopy (JY-HR800, the excitation wavelength of 532 nm). The carbon content in the sample was obtained by thermogravimetric analyzer (STA 6000, PerkinElmer) which worked with a heating rate of 10 °C min^{-1} in air. An ASAP 2020 volumetric adsorption analyzer (Micromeritics, USA) was used at 77 K to obtain the data of porous structure of as-prepared samples. Fourier transform infrared spectroscopy (FTIR) data were obtained by a Thermo Nicolet NEXUS 670. X-ray photoelectron spectroscopy (XPS, PerkinElmer PHI-5702 multifunctional photoelectron spectrometer, Physical Electronics, Chanhassen, USA) was used to study the surface chemical species of the as-prepared samples, and the excitation source was fixed at 1486.6 eV radiation.

Fabrication of Half-Cell and Full-Cell for Ion Capacitors. For the fabrication of anode, active material (MoS_2−C), conducting filler (acetylene black), and the binder (polyvinylidene fluoride (PVDF) in methyl-2-pyrrolidone (NMP) with mass ratio of 8:1:1 were well mixed in a mortar to obtain a black slurry. And then the black slurry was uniformly coated on the current collector (copper foil). After that, the copper foil coated with the black slurry was heated at 110 °C in a vacuum drying oven for 10 h and then pressed by a hydraulic machine with a pressure of 5 MPa and punched into 12 mm diameter round electrodes. The mass loading of active material on round electrode is about 0.8−1 mg. In addition, some round electrodes with the low mass loading of active materials (about 0.1 mg) was fabricated via the above method, which were used to study the kinetics mechanism of Na^+ storage for these MoS_2−C electrodes. After that, all anodes were transferred into the glovebox filled with Ar for further use. For the fabrication of cathode, a homemade polyaniline derived porous carbon (PDPC) was mixed with the binder PTFE with a mass ratio of 9:1 in a mortar and then rolled into thin sheets. The thin sheet was heated at 80 °C for 10 h and then cut into a rectangle shape. The rectangle sheet was pressed on Al foil current collector by a hydraulic machine with a pressure of 5 MPa. And then the PDPC cathodes were dried in a vacuum drying oven at 160 °C for 10 h. After that, the PDPC cathodes were transferred into glovebox filled with Ar for further use.

In this work, two-electrode standard method was employed to study the electrochemical performance of the as-obtained material. The electrolyte is $NaClO_4$ (1 M) based organic solution that is composed of ethylene carbonate/diethyl carbonate/fluoroethylene carbonate (EC/DEC/FEC) (1:1:0.05 v/v/v). For half cells, both anode and cathode were studied in the 2032 type coin cells. In half cells, the reference and counter electrode is Na metal foil; the separator is a round glass-fiber membrane (Whatman). Before the fabrication of sodium-ion capacitors (SICs), MoS_2−C anode was charged/discharged for 5−10 cycles and ended at 3.0 V using a low current density of 0.1 A g^{-1}. A desodiated MoS_2−C coupled with a PDPC cathode was assembled in a 2032 type coin cell, which was separated by a round glass-fiber membrane.

Electrochemical Measurements. Electrochemical workstations, such as CHI660E (Shanghai Chenhua, China) and Autolab PGSTAT 302N (Metrohm, Switzerland), were employed to carry out the cyclic voltammetry (CV), chronopotentiometry tests and electrical impedance spectroscopy (EIS) studies. A Land CT2001A model battery test system (Wuhan Land Electronics. Ltd., China) was used to test the cycle life and rate capability for half-cells and SICs.

The following equation was used to evaluate the specific capacitance (C, F g^{-1}) of as-assembled SIC:

$$C = I/[(\mathrm{d}E/\mathrm{d}t)m] \approx I/[(\Delta E/\Delta t)m] \quad (1)$$

where I is charge/discharge current, ΔE represents the voltage change after a full discharge, Δt is the time period for a full discharge, and m indicates the mass of the corresponding active electrode material.

The following equation was used to calculate to the energy density (E, Wh kg^{-1}) of as-assembled SIC:

$$E = \int_{V_1}^{V_2} CV \, \mathrm{d}V \quad (2)$$

where V_2 is the upper cell voltage and V_1 is the lower cell voltage.

DOI: 10.1021/acsami.7b09813
ACS Appl. Mater. Interfaces 2017, 9, 32745−32755

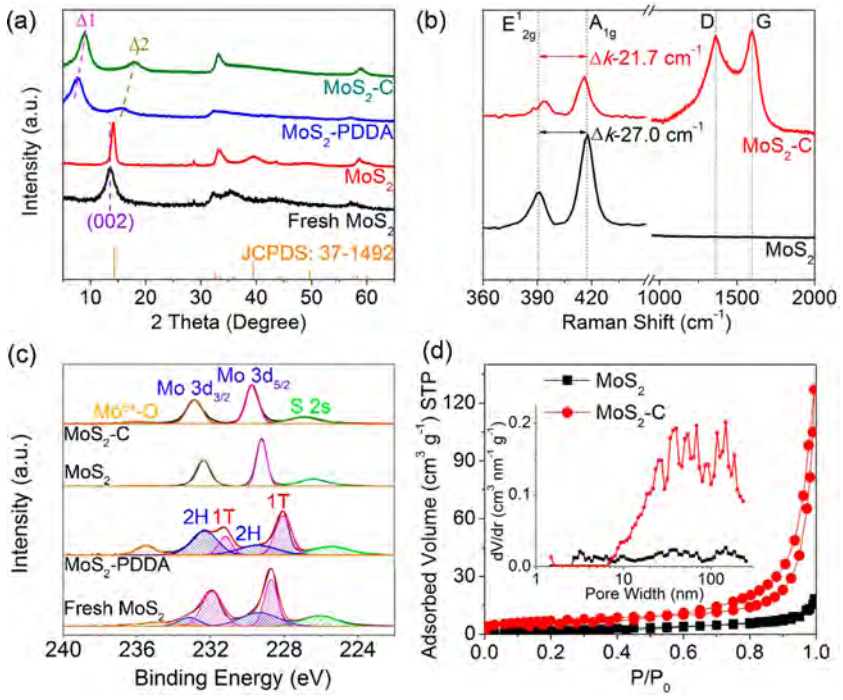

Figure 1. Structural and surface analysis of as-prepared MoS_2 based sample: (a) XRD patterns; (b) Raman spectra; (c) XPS spectra of Mo 3d; (d) N_2 sorption isotherms and inset showing the corresponding pore-size distribution curves.

The following equation can be used to calculate to the power density (P, W kg^{-1}) of as-assembled SIC:

$$P = E/t \quad (3)$$

RESULTS AND DISCUSSION

MoS_2−carbon (MoS_2−C) monolayer interoverlapped superstructure is synthesized by an interlayer-modification route, and the details are described in the Experimental Section. Figure 1a shows the X-ray diffraction (XRD) patterns for as-prepared MoS_2 based samples. The major reflections of the annealed MoS_2 without the addition of PDDA match with JCPDS No. 37-1492 for 2H-MoS_2. As compared to the annealed MoS_2, the (002) peak of fresh MoS_2 slightly shifts down, corresponding to a slightly expanding layer spacing of 0.67 nm. The (002) peaks for fresh MoS_2 and the annealed MoS_2 sample are associated with the adjacent MoS_2 monolayers. For the fresh MoS_2−PDDA sample, two new peaks around 7.68° (Δ1) and 15.82° (Δ2) with diploid relationship arise at relatively low-angle area, which can be assigned to (001) and (002) reflections, respectively.[37−40] The calculated d-spacings of the (001) and (002) reflection peaks for MoS_2−PDDA are approximate 11.5 and 5.6 Å, respectively, which suggest that PDDA molecules insert into the adjacent MoS_2 monolayers, rendering the formation of interlayer expanded MoS_2 structure. After annealing at 800 °C, PDDA turns into amorphous carbon. The amorphous carbon likely remains in the adjacent MoS_2 monolayers, which is confirmed by two peaks with diploid relationship also observed in the MoS_2−C composite. The calculated d-spacings of the (001) and (002) reflection peaks for MoS_2−C are approximate 9.86 and 4.90 Å, respectively. Li et al. suggested that an ideal MoS_2−carbon monolayer interoverlapped hierarchical architecture has a basal spacing of 0.98 nm (0.64 + 0.34 nm) in view of the ideal thickness of MoS_2 monolayer and carbon monolayer are 0.64 and 0.34 nm, respectively.[32,40] The 9.86 Å interlayer distance (001) of as-prepared MoS_2−C hybrid matches well with the above suggested value, and the 4.90 Å interlayer distance (002) of as-prepared MoS_2−C hybrid can be associated with the distance between MoS_2 monolayer and carbon monolayer.[40]

Figure S1 in Supporting Information shows the FTIR spectra of the pure PDDA and the as-prepared MoS_2 based samples. Compared with fresh MoS_2 without and with the PDDA addition, one characteristic peak centered at 1466 cm^{-1} in MoS_2−PDDA sample can be assigned to C−N bond,[41] indicating the existence of PDDA molecules. FTIR spectra of MoS_2−C sample displays some strong peaks around 3419, 1638, 1217, and 1049 cm^{-1}, which are attributed to −OH, C═C, C−O−C, and C−O stretching vibrations,[41] respectively; however, no similar peaks are observed in the annealed MoS_2 sample. This FTIR results indicate the formation of amorphous carbon after the heat treatment. Figure 1b shows Raman spectra of bare MoS_2 and MoS_2−C. Two distinct peaks at around 394.1 and 415.8 cm^{-1} are observed in MoS_2−C, which can be ascribed to the in-plane Mo−S phonon mode (E^1_{2g}) and the out-of-plane Mo−S mode (A_{1g}) of layered MoS_2, respectively.[37,38,42,43] Two characteristic peaks at around 1355 and 1597 cm^{-1} are detected in the MoS_2−C sample, which can be assigned to D-band and G-band of carbon material, respectively.[37,38,42,43] Raman spectra of MoS_2−C are obviously different from that of bare MoS_2 where only two peaks of Mo−S vibrations are detected.[42,43] The frequency difference (Δk) between E^1_{2g} and A_{1g} for MoS_2−C sample is about 21.7 cm^{-1} as compared with 27.0 cm^{-1} for pure MoS_2 sample. It is interesting that the Δk value for MoS_2−C samples is close to the reported values (20.2−21.2 cm^{-1}) of MoS_2 with monolayer structure, which may be used to confirm that the MoS_2 sheets in the composite are approximately single-layered or few-layered.[37,42,43] In contrast, the Δk value of MoS_2 sample is close to commercial bulk-state MoS_2 with multilayered structure.[42] The I_D/I_G intensity ratio for MoS_2−C sample is calculated to be

DOI: 10.1021/acsami.7b09813
ACS Appl. Mater. Interfaces 2017, 9, 32745−32755

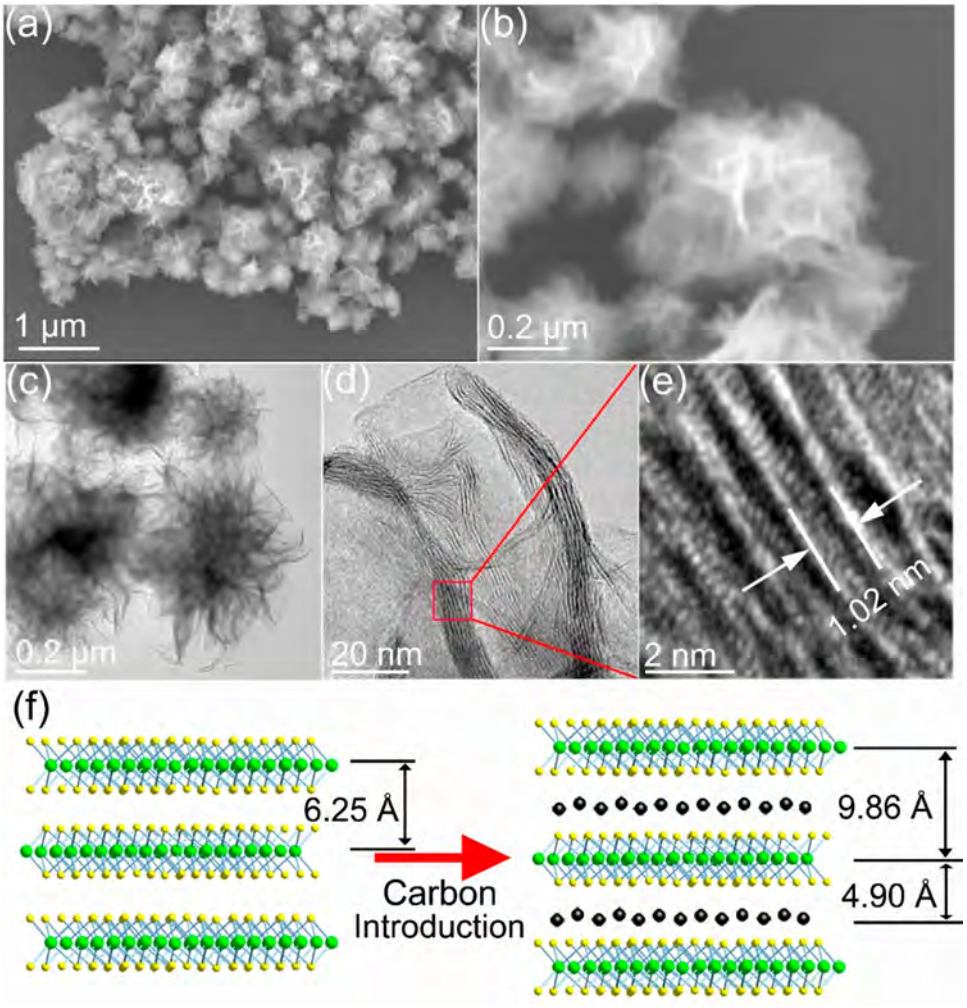

Figure 2. Structure and morphology of as-prepared MoS_2−C sample: (a, b) SEM images; (c, d) TEM and (e) high-resolution TEM images. (f) Schematic illustration of microstructures of layered MoS_2 (left) and MoS_2−C (right) monolayer interoverlapped superstructure.

about 1.27, which suggests that amorphous carbon is formed through the pyrolysis of PDDA which may restrain the stacking of MoS_2 (002) planes to promote the formation of MoS_2 monolayer in the composite.[28,33,37,40] The mass loading of amorphous carbon in MoS_2−C composite is about 25 wt % via thermogravimetric analysis (Figure S2). The carbon content of 25 wt % for our MoS_2−C composite is close to the theoretical value (20 wt %) for MoS_2-graphene interoverlapped superstructures in which the graphene and MoS_2 monolayers are alternately sandwiched.[28]

Figure 1c shows the typical Mo core level XPS spectra of the as-prepared MoS_2-based samples. The spectrum of the MoS_2−PDDA sample displays a couple of doublet peaks at 232.3 eV for Mo $3d_{3/2}$ and 229.4 eV for Mo $3d_{5/2}$ corresponding to 2H-MoS_2, and another couple of doublet peaks around 231.2 eV for Mo $3d_{3/2}$ and 228.1 eV for Mo $3d_{5/2}$ corresponding to 1T MoS_2.[28] In addition, a distinct peak at high binding energy of 235.5 eV is also observed, which can be assigned to Mo^{6+}−O, and a peak arises at 225.4 eV, which can be assigned to S 2s.[28] Fresh MoS_2 without the addition of PDDA shows a similar spectral profile with MoS_2−PDDA. After annealing, the Mo 3d spectrum of the obtained MoS_2−C shows two prominent peaks at 232.9 and 229.7 eV. These two peaks of MoS_2−C can be considered as the Mo $3d_{3/2}$ and Mo $3d_{5/2}$ of 2H-MoS_2. No obvious Mo signal for 1T-MoS_2 is observed, thus indicating that the 1T-MoS_2 is effectively turned into stable 2H-MoS_2 after annealing.[28] We find that the Mo 3d peak position of MoS_2−C shifts slightly to higher binding energy as compared to MoS_2 sample, which is probably because of the partial oxidation on the surface during thermal treatment. Figure S3 shows the S 2p core level spectra of the MoS_2 based samples. Two distinct peaks are present in all samples, which can be assigned to S $2p_{1/2}$ (Δ) and S $2p_{3/2}$ (∇), suggesting the existence of S^{2-}.[28,39] Isotherms from Brunauer−Emmet−Teller (BET) characterization data (Figure 1d) show that both MoS_2 and MoS_2−C show the type H3 loops, indicating the MoS_2 and MoS_2−C comprise loose assemblages of platelike MoS_2 forming slitlike pores. Two identical pore-size distribution curves (Figure 1d inset) are observed for MoS_2 and MoS_2−C samples, suggesting the difference in sheet assembled structures between MoS_2 and MoS_2−C samples. Notably, the specific BET surface area of MoS_2−C composite is about 24.4 $m^2\ g^{-1}$, which is much higher than that of MoS_2 (10.2 $m^2\ g^{-1}$).

Scanning electron microscopy (SEM) and transmission electron microscopy (TEM) were employed to characterize the morphology and microstructure of bare MoS_2 and MoS_2−C samples. The MoS_2−C composite features microflower-like morphology that is assembled by ultrathin MoS_2 nanosheets (Figure 2a−c), which is consistent with BET characterization. Figure 2d and Figure 2e show that the thickness of individual

DOI: 10.1021/acsami.7b09813
ACS Appl. Mater. Interfaces 2017, 9, 32745−32755

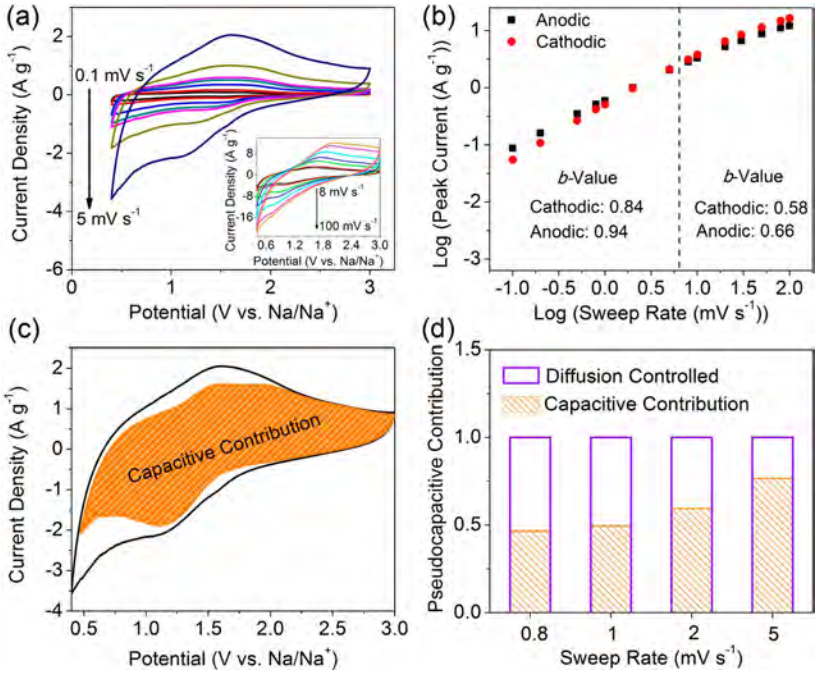

Figure 3. Electrochemical kinetics analysis of MoS_2−C electrode: (a) CV curves of MoS_2−C at various scan rates for 0.1−100 mV s^{-1}; (b) determination of the *b*-value using the relationship between anodic/cathodic peak current and scan rate; (c) separation of the capacitive and diffusion currents in MoS_2−C at a scan rate of 5 mV s^{-1}, respectively; (d) contribution ratio of the capacitive charge versus scan rate.

MoS_2 nanosheets is less than 10 nm and the interlayer spacing between adjacent MoS_2 monolayers for MoS_2−C sample is around 10.2 Å, which is consistent with the XRD characterizations. In comparison, MoS_2 sample is in bulk state (Figure S4a−c) agglomerated by thick MoS_2 nanosheets and has an interlayer spacing of 6.25 Å (Figure S4d and Figure S4e).

Accordingly, the formation of the MoS_2−C superstructures monolayer interoverlapped superstructure may be related to the PDDA insertion into MoS_2 layers. PDDA, as a cationic polyelectrolyte,[38] can be easily coated on MoS_2 layers in the hydrothermal process. Diploid relationship observed in XRD pattern of MoS_2−PDDA confirms that PDDA is inserted into MoS_2 monolayers to form the interoverlapped structure. Similar XRD diploid relationship was also reported in MoS_2-octylamine,[28] MoS_2-poly(ethylene oxide) (PEO),[30] and MoS_2-oleylamine interoverlapped structures.[40] PDDA, just as other organics,[28,30,40] tends to play a pillar role in maintaining the MoS_2 layers in expansion. After the annealing, PDDA transforms into amorphous carbon which likely exists in the adjacent MoS_2 monolayers. This is confirmed by the above structural and spectral analyses. In addition, linear scan EDS mappings in Figure S5 show that the curves of C−K, Mo−K, and S−K feature a similar profile, indicating the uniformly distribution of these elements. While MoS_2−C composite has about 25 wt % carbon content, no obvious carbon layer is observed from the edges of the nanosheets (Figure 2d). In short, the above results establish that amorphous carbon (derived from PDDA) can be intercalated between the adjacent MoS_2 monolayers to form a 2D atomic interoverlapped hierarchical architecture as depicted in Figure 2f.

To investigate the Na^+ ion charge storage properties of as-prepared MoS_2−C sample, half-cells were employed (details seen in Experimental Section). Figure 3a depicts the typical CV curves of MoS_2−C composites at a wide range of sweep rates. Charge storage occurs mainly by the insertion/desertion of Na^+ ions into/out of the interlayer site to form sodiated MoS_2 (Na_xMoS_2, x_{max} = 2).[25−27]

$$MoS_2 + xNa^+ + xe^- \rightarrow Na_xMoS_2 \quad (4)$$

These CV curves feature similar profiles with some broad peaks occurring in both anodic and cathodic processes, which are distinguished from current response of bare MoS_2 electrode with several redox peaks (Figure S6a). A pair of broad reversible peaks for MoS_2−C electrode means that this interoverlapped hierarchical architecture has many easily accessible surface-redox active sites caused by synergistic effect between the MoS_2 monolayers and amorphous carbon.[26,29,44] These active sites are considered to be highly defective, which perhaps possess a broad distribution in energies related to surface-redox reactions. Notably, Nb_2O_5 (vs Li^+/Li) and TiO_2 (vs Na^+/Na), which usually can be assigned to pseudocapacitive materials,[45−47] also show a similar broadened electrochemical signature.

CVs in Figure 3a also provide greater insight into the charge storage kinetics of MoS_2−C. In general, the following equation can be used to depict the relationship between the scan rates (v) and peak current (i):[44,45]

$$i = av^b \quad (5)$$

where a and b are appropriate values. Specifically, *b*-value is 0.5, which suggests a diffusion-controlled (or battery-like) behavior caused by slowly semi-infinite linear ion diffusion; *b*-value is 1.0, which indicates a capacitive behavior related to a fast faradaic redox reaction on the surface.[44,45] As the scan rate ranges from 0.1 to 5 mV s^{-1}, the *b*-values for anodic and cathodic peaks of MoS_2−C electrode are 0.94 and 0.84 (Figure 3b), respectively. These *b*-values are close to 1, which suggests that the redox reaction is predominantly surface-controlled. In other words, this is one of characteristic features of pseudocapacitance.[29,44,47] It is likely that as-prepared MoS_2−C inherits the pseudocapa-

DOI: 10.1021/acsami.7b09813
ACS Appl. Mater. Interfaces 2017, 9, 32745−32755

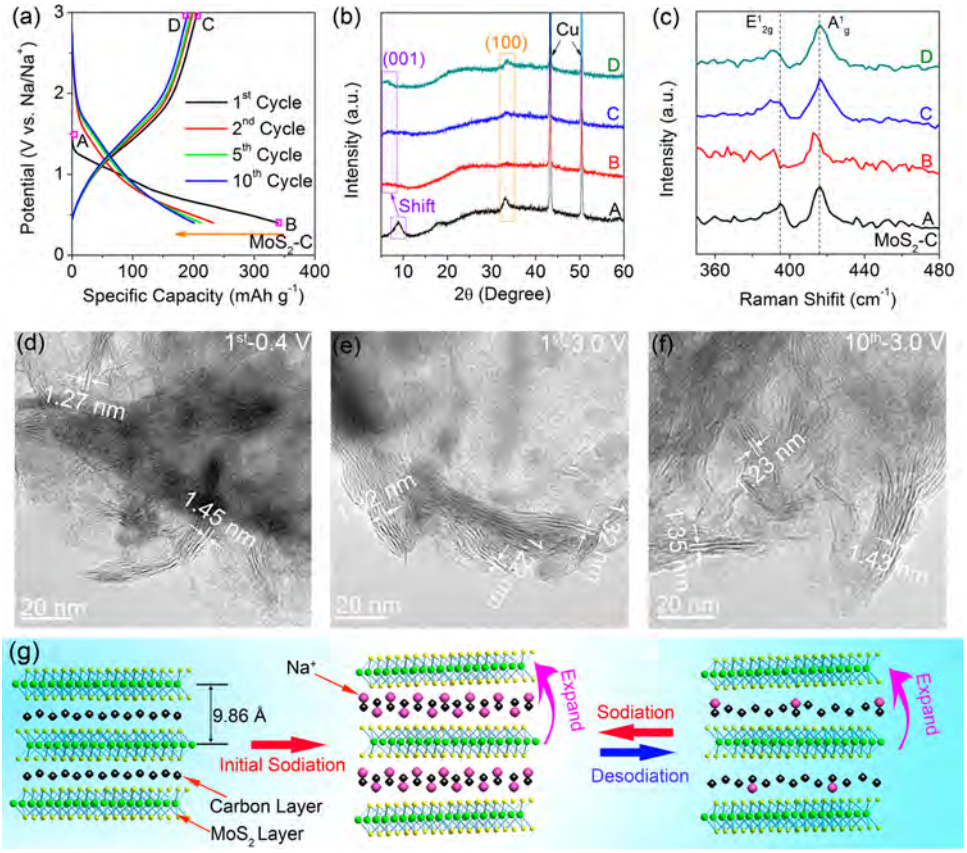

Figure 4. Electrochemical properties and associated structural changes of MoS_2−C. (a) Charge/discharge curves for MoS_2−C at a current density of 0.1 A g^{-1}. (b) Ex situ XRD and (c) Raman patterns for MoS_2−C during the different charging/discharging states: pristine state (A), initial sodiated state (B), initial desodiated state (C), desodiated state after 10 cycles (D). (d−f) HRTEM image of MoS_2−C sample during the initial sodiation to 0.4 V (vs Na/Na^+), during the initial desodiation to 3.0 V (vs Na/Na^+), and after 10 cycles desodiation to 3.0 V (vs Na/Na^+), respectively. (g) Schematic illustration of the reaction mechanism of MoS_2−C by electrochemical activation.

citive properties of bare MoS_2. We noted that the *b*-values for anodic and cathodic peaks of bare MoS_2 electrode are 0.93 and 0.91 (Figure S6b), respectively, confirming the capacitive-like nature of the kinetics of MoS_2, which is consistent with previously reported mesoporous MoS_2 film.[29] A change of slope occurs as the sweep rates are above 8 mV s^{-1} for MoS_2−C electrodes, showing a rapid decrease of *b*-value for anodic and cathodic peaks. This limitation in kinetics at the high sweep rates is associated with some factors, such as an increase in ohmic contribution or a diffusion limitation/constraint.[45,46]

Following Dunn and co-workers' reported approach,[44] it is straightforward to separate the capacitive contribution from the total current response quantitatively via use of the scan rate dependence of CVs. At a fixed potential, the current response (i) can be considered as being composed by the surface capacitive process (k_1v) and the diffusion-controlled (battery-like) Na^+ intercalation ($k_2v^{1/2}$):[44−46]

$$i(V) = k_1v + k_2v^{1/2} \quad (6)$$

Equation 6 can be transformed into

$$i(V)/v^{1/2} = k_1v^{1/2} + k_2 \quad (7)$$

Equation 7 enables us to evaluate the k_1 and k_2 values under the different potentials (V) with ease.[44−46] Figure 3c show the voltage profile of pseudocapacitive currents (shaded area) for MoS_2−C electrodes at a scan rate of 5 mV s^{-1}. Pseudocapacitive contribution ratios for MoS_2−C at the different sweep rates from 0.5 to 5 mV s^{-1} were also investigated. The data in Figure 3d show that the capacitive contribution ratio value increases gradually as the scan rate increases. Finally, the capacitive contribution ratio value is up to 76.7% at 5 mV s^{-1} for MoS_2−C electrodes. In addition, bare MoS_2 electrode also shows the attractive pseudocapacitive contribution ratios (Figure S6c and Figure S6d). Overall, the CVs measurements demonstrated that MoS_2−C has the pseudocapacitive characteristic, suggesting its fast kinetics in nature.

Figure 4a and Figure S7a show the discharge potential profiles of as-prepared MoS_2 based electrodes from 0.4 to 3.0 V (vs Na^+/Na), respectively. Two clear discharge plateaus at around 0.85 and 0.75 V can be well recognized in the initial discharge profile of MoS_2, corresponding to an irreversible first-order phase change from the 2H-MoS_2 phase to the 1T-MoS_2 phase and the formation of SEI.[26,27] In the following charge/discharge curves, the plateaus disappear and become sloped approximation, corresponding to the reversible Na^+ inserted/deserted process into/out of the layers of newly formed 1T-MoS_2.[26,27,48] On the contrary, the discharge/charge curves including the initial and followed cycles of MoS_2−C feature the sloped profile. These plateaus become vague in the initial discharge profile of MoS_2−C due to unique hierarchical architecture at the nanoscale where MoS_2 monolayer and carbon layer were interoverlapped. Other MoS_2 samples in nanoscale with low crystallinity or mesoporous structure also have the similar behavior.[26,29,48] The pseudolinear galvanostatic

DOI: 10.1021/acsami.7b09813
ACS Appl. Mater. Interfaces 2017, 9, 32745−32755

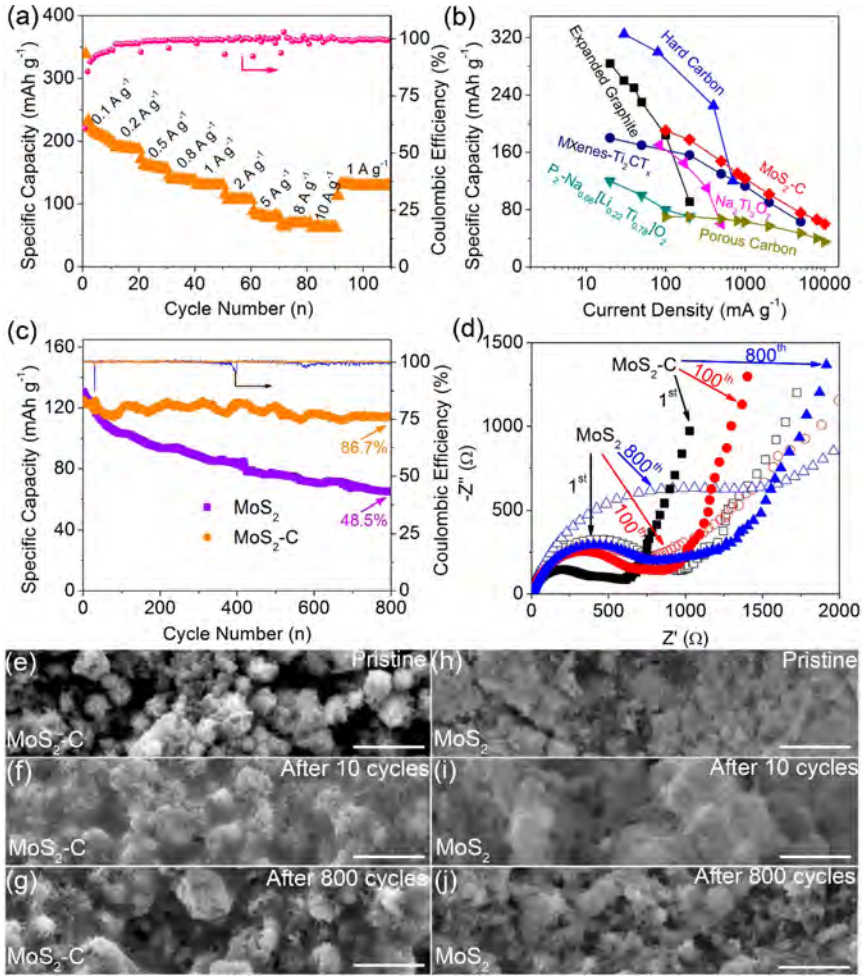

Figure 5. Electrochemical performance of MoS_2−C electrode in a half cell. (a) Rate performance at various current density from 0.1 to 10 A g^{-1}. (b) Rate capability for MoS_2−C compared to other anodes in reported literature: MXenes,[49] hard carbon,[50] expanded graphite,[51] $Na_2Ti_3O_7$,[52] P_2-$Na_{0.66}[Li_{0.22}Ti_{0.78}]O_2$,[53] and homemade porous carbon cathode. (c) Long-term cycling performance at a current density of 1 A g^{-1}. (d) Nyquist plots obtained at 1.0 V (vs Na/Na^+) for MoS_2 and MoS_2−C during the different cycling state. SEM images of the MoS_2−C before (e), after 10 cycles (f), and after 800 cycles (g). SEM images of the MoS_2 before (h), after 10 cycles (i), and after 800 cycles (j). Scale bar in SEM images: 1 μm.

traces are found in MoS_2−C and bare MoS_2 electrodes, suggesting the pseudocapacitive characteristics.

To further confirm the pseudocapacitive characteristics of MoS_2−C, ex situ XRD and Raman spectroscopy were used. Before the study of MoS_2−C, the structure change of MoS_2 was first evaluated (Figure S7b,c). After the initial insertion of Na^+, the (002) diffraction peak of MoS_2 down-shifts to 9.28 Å and a new peak located at 4.64 Å is observed (Figure S7b), directly confirming the phase transition from the phase of semiconducting 2H-MoS_2 to the metallic 1T-MoS_2.[7,26,29] The newly formed peaks may be associated with adjacent structure between inserted Na^+ and MoS_2 layer, which is similar to MoS_2−C with an interoverlapped carbon layer−MoS_2 layer structure and other interoverlapped MoS_2 structure.[34,37,40] As linear EDX confirms Na atom exists in MoS_2 (Figure S8), Na^+ is definitely intercalated/adsorbed in or on the MoS_2 sheets electrochemically.[49] Ex situ Raman spectra in Figure S7c shows that E^1_{2g} and A_{1g} characteristic peaks for MoS_2 are still preserved, confirming that S−Mo−S layer structure in MoS_2 is not damaged. The expansion of interlayer distance is about 3.0 Å based on the shift of the (002) diffraction peak, which is consistent with other reports.[26,29,49] HRTEM images (Figure S7d) also confirmed this expansion. After MoS_2 electrode was charged to 3.0 V or even charged/discharged with 10 cycles, the ex situ XRD and Raman pattern profiles had no obvious change as compared with initial intercalated state of Na^+. A small upshift for peak from 9.28 to 9.09 Å is observed, corresponding to a change in the interlayer distance within 0.19 Å. It is interesting that the newly formed peak has no change after MoS_2 electrode was charged to 3.0 V or even after 10 cycles. The residual Na^+ is detected, which looks like a pillar supporting the MoS_2 monolayers and thus rendering the interlayer distance unchanged. The residual Na^+ phenomenon is also observed in other works about Li^+ and Na^+ inserted/deserted MoS_2[7,29] or other 2D materials such as MXenes.[49] Ann et al. suggested that the residual Na^+ in MoS_2 layers is about 0−0.15 mol after desodiation.[27] The residual Na^+ is also detected by linear energy-dispersive X-ray spectroscopy (EDS) analysis (Figure S8).

In contrast, following sodiation, the XRD pattern (Figure 4b) of MoS_2−C becomes mostly featureless, with the (001) and (002) diffraction peaks disappearing. Instead a few faint (or broad) peaks are shifted from the peak position of the parent material. The broadness of the shifted (001) peak indicates that the nanosheets are randomly arranged during sodiation with large spacing between the layers.[7] Although the crystallographic

DOI: 10.1021/acsami.7b09813
ACS Appl. Mater. Interfaces 2017, 9, 32745−32755

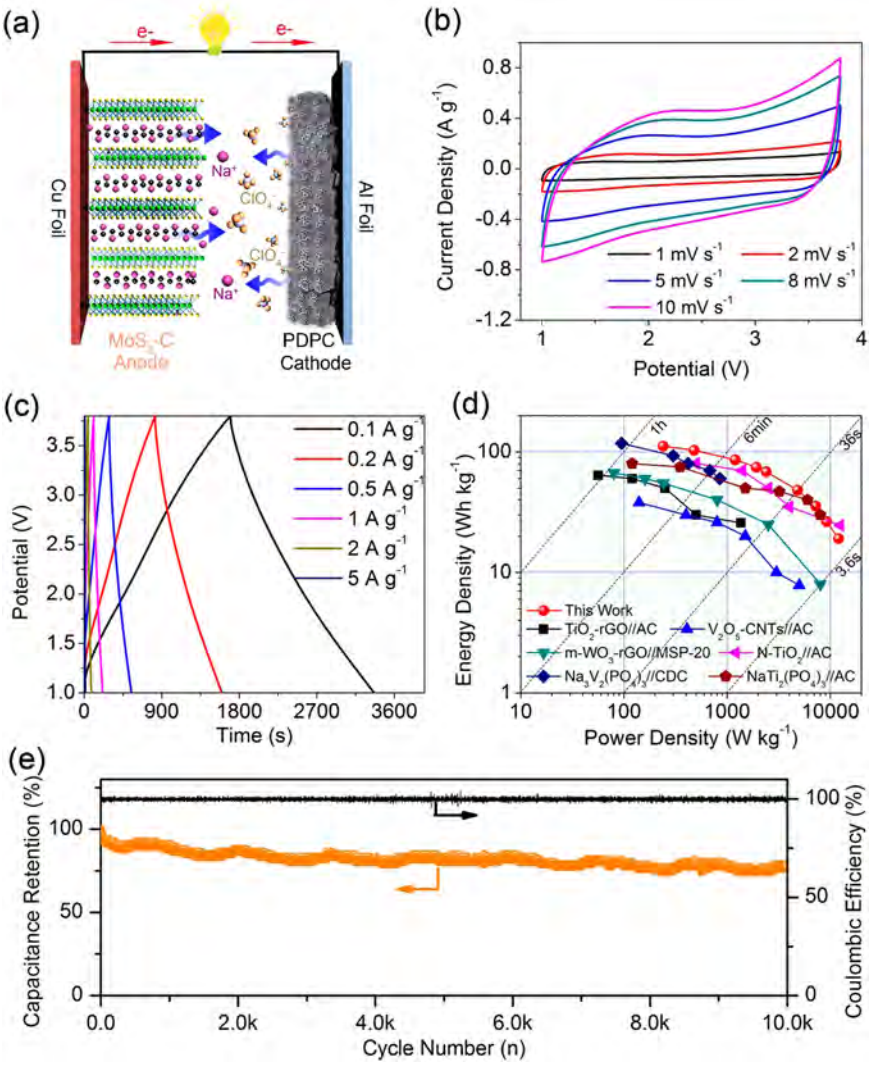

Figure 6. Performance of the prototype sodium-ion capacitor (SIC) full cell: (a) schematic illustration of this SIC during the discharge; (b) CVs of as-fabricated SIC at various scan rates from 1 to 10 mV s^{-1}; (c) charge/discharge curves of as-fabricated SIC at the different current densities from 0.1 to 5 A g^{-1}; (d) Ragone plots of SIC in this work compared to representative SICs in literature; (e) cycling stability for 10 000 cycles at a current density of 2 A g^{-1} and the corresponding Coulombic efficiency of 100%.

order of MoS_2−C becomes poor and is similar to the amorphous phase, ex situ Raman spectra in Figure 4c shows that E^1_{2g} and A_{1g} characteristic peaks for MoS_2 are still preserved, confirming that S−Mo−S layer structure in MoS_2−C is not damaged. HRTEM characterization (Figure 4d) further demonstrates that S−Mo−S layer structure is still preserved and the interlayer spacing between adjacent S−Mo−S layers for MoS_2−C sample is expanded more than 14 Å after sodiation. As linear EDS confirms Na existing in MoS_2−C (Figure S9), Na^+ is definitely intercalated/adsorbed in or on the MoS_2−C electrochemically.[49] On the basis of the above discussions from the ex situ XRD, Raman, HRTEM, and linear EDS taken together, it appears that MoS_2−C also undergoes the layer-expansion process, which is similar to MoS_2 during initial sodiation. After desodiation and 10 charged/discharged cycles, the spectral profile of XRD and Raman shows no obvious change, which indicates that the MoS_2−C (after sodiation) does not undergo a phase transformation. The residual Na^+ detected by linear EDS (Figure S9) and amorphous carbon layer may come together to behave as pillars between the MoS_2 monolayers, rendering the interlayer distance in expansion (Figure 4e,f).[49] The MoS_2 layers with different expanding spacings are observed in Figure 4d−f, which may be associated with that the formation of a distorted structure caused by irregular arrangement of MoS_2 layers.[48] Therefore, the reaction mechanism of MoS_2−C and MoS_2 can be illustrated in Figure 4g and Figure S10 during sodiated/desodiated process, respectively. Specifically, Na^+ is intercalated between the layers of MoS_2−C in nonaqueous electrolyte with the interlayer distance (001) expanding from 9.86 Å to the larger values (over 1.25 Å) during the initial sodiation. Then, Na^+ can reversibly insert into and desert out the interlayer space of MoS_2−C with a negligible change in the interlayer distance. In the deintercalation process, residual Na^+ is detected, which may play a pillar role in maintaining the interlayer distance in expansion.[48,49] Obviously, MoS_2−C undergoes an irreversible structure (or layer) change process during the initial sodiation. And yet, the interlayer distance of MoS_2−C is expanded significantly large enough that a phase or structure transition is no longer energetically needed to accommodate sodium into the structure.[29,48,49] Thus, MoS_2−C becomes the pseudocapacitance-type material in the

DOI: 10.1021/acsami.7b09813
ACS Appl. Mater. Interfaces 2017, 9, 32745−32755

nonaqueous Na^+ electrolyte with no significant shrinkage/expansion of the interlayer distance in the following sodiated and desodiated process.

The rate capability and cycle life of MoS_2−C were further characterized. At 0.1 A g^{-1}, MoS_2−C can deliver a high specific capacity value of 200 mAh g^{-1} (from 10th cycle) (Figure 5a). Furthermore, MoS_2−C delivers 62 mAh g^{-1} even at a large current density of 10 A g^{-1}, approximately 31% of initial specific capacity obtained from 0.1 A g^{-1}. The excellent rate capability underscores the pseudocapacitive nature of charge storage in MoS_2−C. Figure S11 shows that MoS_2−C has a good rate capability as compared to bare MoS_2. In addition, it is also higher than that of MoS_2−PDDA (Figure S12) and other ion intercalation electrodes (Figure 5b), such as MXenes,[49] hard carbon,[50] expanded graphite,[51] $Na_2Ti_3O_7$,[52] P2-$Na_{0.66}[Li_{0.22}Ti_{0.75}]O_2$.[53]

Figure 5c shows that the cycling behavior of MoS_2−C is more stable than that of MoS_2. After 800 constant charged/discharge cycles (1 A g^{-1}), the capacity decreased by only 13.3% for MoS_2−C, in contrast to the 51.5% decay exhibited by the MoS_2. Moreover, MoS_2−C also exhibited a good cycling performance over 5000 cycles at a large current density of 5 A g^{-1} (Figure S13). It can be observed that the increment of specific capacity of MoS_2−C material during the cycling as shown in Figure S13, which may be associated with the interoverlapped carbon layer−MoS_2 layer structure of MoS_2−C, is fully expanded (or activated) after the initial cycles, thus providing more active sites for sodiation or desodication.[48,49] This behavior indicates that by introducing amorphous carbon into adjacent MoS_2 monolayers to form the interoverlapped hierarchical architecture, it is possible to improve the cycling stability of MoS_2, a feature that has been a significant limitation in the application of this material in sodium-ion batteries and SICs.

As discussed above, it is not at all clear, however, how MoS_2−C with an interlayer-expanded structure could have the high cycling stability. To examine this issue, electrochemical impedance spectroscopy (EIS) was performed on both MoS_2−C and MoS_2 at the same potential of 1.0 V (vs Na/Na^+) under the different cycling stages. The Nyquist plots are presented in Figure 5d. In low frequency region, the straight line is related to the diffusion of the ions.[54−56] In high and middle frequency regions, the depressed semicircle can be attributed to two overlapped interface impendances caused by charge transfer and SEI.[54,55] In low-frequency region, the slightly change of inclined line in MoS_2−C after 800 cycles suggests that the fast Na^+ diffusion property is preserved even after the long cycling period, whereas the inclined line at low frequency of MoS_2 undergoes an obvious change. In addition, MoS_2−C experienced a slight increase of interface impedance after 800 cycles as compared to a large increase for MoS_2, most likely due to the stable SEI coated on the surface of MoS_2−C.[54−56]

Furthermore, SEM was employed to characterize the SEI on the electrodes before and after cycles. Figure 5e−g show that the SEI can be uniformly coated on the MoS_2−C electrode after 10 cycles and still preserved after 800 cycles, which is consistent with slightly changed interface impedance from EIS characterization. On the contrary, uniform SEI forms on the MoS_2 electrode after 10 cycles; however, it will become rough and highly inhomogeneous after 800 cycles (Figure 5h−j), corresponding to largely increased interface impedance for MoS_2. Furthermore, Figure S14 shows that MoS_2−C composite preserved the pristine layer structure after long cycles. Therefore, the stable existing SEI and little change in Na ion transport properties provide viable evidence for achieving higher cycling stability in MoS_2−C. Our results indicate that MoS_2−C has the excellent Na^+ charge storage properties in rate capability and long cycle life. Therefore, it is highly realistic that MoS_2−C can be used as a practical anode material for sodium-ion based energy storage devices.

To further demonstrate the potential of MoS_2−C monolayer interoverlapped structure in sodium-ion capacitors, a prototype full cell as shown in Figure 6a was fabricated by using MoS_2−C as an anode electrode and a homemade polyaniline derived porous carbon (PDPC) as a cathode electrode in $NaClO_4$ based organic electrolyte. More structure information on PDPC can be found in our previous work.[57] We also demonstrate that PDPC can operate within a potential range of 3−4.2 V (vs Na/Na^+; Figure S15) and deliver a high specific capacity of 70 mAh g^{-1} at 0.2 A g^{-1} and even work at a high rate. The working potential window for a full cell can reach up to 3.8 V with regard to the difference in working potential window between anode (0.4−3 V vs Na/Na^+) and cathode (3−4.2 V vs Na/Na^+). Furthermore, to avoid the risk of electrolyte decomposition and other side reactions, the working voltage window of full cell is set between 1 and 3.8 V.[20,47,58,59] The mass ratio of anode and cathode active materials was optimized to 1:2 in terms of the charge balance and electrochemical performance (Figure S16).[11,14,20,55] Figure 6b and Figure 6c show the near-rectangular CVs curves and the symmetric linear charge−discharge profiles, respectively, suggesting a typical capacitive behavior for the assembled MoS_2−C//PDPC full cell.[55] The energy and power densities (based on the mass of active materials in SIC) can be evaluated from the charge/discharge curves in Figure 6c. A high energy density of 111.4 Wh kg^{-1} can be obtained at a power density of 240 W kg^{-1}. It should also be pointed out that this full cell still achieved an energy density of 19.1 Wh kg^{-1} at an extremely high power density of 12 000 W kg^{-1}. As shown in Figure 6d, the energy/power densities of the as-assembled SIC are higher than several representative SICs.[25,47,60−63] Furthermore, this SIC preserves ∼77.3% of its initial capacitance even after 10 000 cycles at a large current density of 2 A g^{-1} (Figure 6e), which indicates that this hybrid SIC is also very stable with a high Columbic efficiency.

CONCLUSIONS

MoS_2−C nanocomposite with monolayer interoverlapped superstructure has a highly reversible capacity of 200 mAh g^{-1} at 100 mA g^{-1}. Even at a high rate of 10 000 mA g^{-1}, 62 mAh g^{-1} can be achieved. Most importantly, MoS_2−C nanocomposite exhibits an ultralong cycle life over 5000 cycles. Electrochemical kinetics analysis reveals that Na^+ can insert into and desert out the interoverlapped structure of MoS_2−C via a pseudocapacitive-dominant process, as confirmed by ex situ XRD, Raman, and TEM characterizations. This fast kinetics and unique monolayer interoverlapped architecture, therefore, are highly beneficial to high rate and long cycle life of MoS_2−C composite. When such high-performance MoS_2−C composite was used as an anode for SICs, the electrochemical performance was extraordinary. This SIC can deliver an energy density of 111.4 Wh kg^{-1} at a power density of 240 W kg^{-1} and more than 19 Wh kg^{-1} at an extremely high power density of 12 000 W kg^{-1} as well as an excellent cycling stability (exceeding 10 000 cycles). Our findings presented here will provide a new route for developing high-performance anode materials for SICs or even SIBs with high rate and long cycle life.

DOI: 10.1021/acsami.7b09813
ACS Appl. Mater. Interfaces 2017, 9, 32745−32755

■ ASSOCIATED CONTENT

Supporting Information

The Supporting Information is available free of charge on the ACS Publications website at DOI: 10.1021/acsami.7b09813.

FTIR, TGA, S 2p XPS, SEM, TEM characterizations for MoS_2−C and MoS_2 samples; electrochemical kinetics analysis of MoS_2 electrode and the corresponding structure change by TEM; EDS analysis of MoS_2−C and MoS_2 samples during the sodiation and desodiation state; schematic illustration of the sodium intercalated reaction mechanism of MoS_2; rate performance, cycling test, and Nyquist plot of MoS_2 and MoS_2−PDDA; electrochemical characterizations on PDPC; electrochemical performance of MoS_2−C based on SIC with different cathode/anode mass ratios (PDF)

■ AUTHOR INFORMATION

Corresponding Author

*E-mail: lizhang@mae.cuhk.edu.hk.

ORCID

Li Zhang: 0000-0003-1152-8962

Author Contributions

The manuscript was written through contributions of all authors. All authors have given approval to the final version of the manuscript.

Notes

The authors declare no competing financial interest.

■ ACKNOWLEDGMENTS

This work was supported by HKSAR Innovation and Technology Commission (ITC; Project ITS/160/14FP) and the General Research Fund (GRF) from the Research Grants Council (RGC) of Hong Kong with Projects 14209514 and 14203715. R.W. was supported by Postdoctoral Fellow Scheme from Faculty of Engineering, The Chinese University of Hong Kong. We also thank Wai-kit Mok (Allan), Man Hau Yeung, and Chi-Ming Cheuk for TEM, SEM, and XRD studies.

■ REFERENCES

(1) Salanne, M.; Rotenberg, B.; Naoi, K.; Kaneko, K.; Taberna, P.-L. C.; Grey, P.; Dunn, B.; Simon, P. Efficient Storage Mechanisms for Building Better Supercapacitors. *Nat. Energy* **2016**, *1*, 16070.

(2) Lukatskaya, M. R.; Dunn, B.; Gogotsi, Y. Multidimensional Materials and Device Architectures for Future Hybrid Energy Storage. *Nat. Commun.* **2016**, *7*, 12647.

(3) Gogotsi, Y.; Simon, P. True Performance Metrics in Electrochemical Energy Storage. *Science* **2011**, *334*, 917−918.

(4) Naoi, K.; Ishimoto, S.; Miyamoto, J. − I; Naoi, W. Second Generation 'Nanohybrid Supercapacitor': Evolution of Capacitive Energy Storage Devices. *Energy Environ. Sci.* **2012**, *5*, 9363−9373.

(5) Wang, G.; Zhang, L.; Zhang, J. A Review of Electrode Materials for Electrochemical Supercapacitors. *Chem. Soc. Rev.* **2012**, *41*, 797−828.

(6) Zhu, Y.; Murali, S.; Stoller, M. D.; Ganesh, K. J.; Cai, W.; Ferreira, P. J.; Pirkle, A.; Wallace, R. M.; Cychosz, K. A.; Thommes, M.; Su, D.; Stach, E. A.; Ruoff, R. S. Carbon-Based Supercapacitors Produced by Activation of Graphene. *Science* **2011**, *332*, 1537−1541.

(7) Acerce, M.; Voiry, D. M.; Chhowalla, M. Metallic 1T Phase MoS_2 Nanosheets as Supercapacitor Electrode Materials. *Nat. Nanotechnol.* **2015**, *10*, 313−318.

(8) Pomerantseva, E.; Gogotsi, Y. Two-Dimensional Heterostructures for Energy Storage. *Nat. Energy* **2017**, *2*, 17089.

(9) Aravindan, V.; Gnanaraj, J.; Lee, Y.-S.; Madhavi, S. Insertion-Type Electrodes for Nonaqueous Li-Ion Capacitors. *Chem. Rev.* **2014**, *114*, 11619−11635.

(10) Ma, Y.; Chang, H.; Zhang, M.; Chen, Y. Graphene-Based Materials for Lithium-Ion Hybrid Supercapacitors. *Adv. Mater.* **2015**, *27*, 5296−5308.

(11) Khomenko, V.; Raymundo-Piñero, E.; Béguin, F. High-Energy Density Graphite/AC Capacitor in Organic Electrolyte. *J. Power Sources* **2008**, *177*, 643−651.

(12) Ni, J.; Huang, Y.; Gao, L. A High-Performance Hard Carbon for Li-ion Batteries and Supercapacitors Application. *J. Power Sources* **2013**, *223*, 306−311.

(13) Leng, K.; Zhang, F.; Zhang, L.; Zhang, T.; Wu, Y.; Lu, Y.; Huang, Y.; Chen, Y. Graphene-Based Li-ion Hybrid Supercapacitors with Ultrahigh Performance. *Nano Res.* **2013**, *6*, 581−592.

(14) Luo, J.; Zhang, W.; Yuan, H.; Jin, C.; Zhang, L.; Huang, H.; Liang, C.; Xia, Y.; Zhang, J.; Gan, Y.; Tao, X. Pillared Structure Design of MXene with Ultralarge Interlayer Spacing for High Performance Lithium-ion Capacitors. *ACS Nano* **2017**, *11*, 2459−2469.

(15) Kong, L.; Zhang, C.; Wang, J.; Qiao, W.; Ling, L.; Long, D. Free-Standing T-Nb_2O_5/Graphene Composite Papers with Ultrahigh Gravimetric/Volumetric Capacitance for Li-ion Intercalation Pseudocapacitor. *ACS Nano* **2015**, *9*, 11200−11208.

(16) Lim, E.; Kim, H.; Jo, C.; Chun, J.; Ku, K.; Kim, S.; Lee, H. I.; Nam, I. − S.; Yoon, S.; Kang, K.; Lee, J. Advanced Hybrid Supercapacitor Based on a Mesoporous Niobium Pentoxide/Carbon as High-performance Anode. *ACS Nano* **2014**, *8*, 8968−8978.

(17) Aravindan, V.; Ulaganathan, M.; Madhavi, S. Research Progress in Na-ion Capacitors. *J. Mater. Chem. A* **2016**, *4*, 7538−7548.

(18) Choi, J. W.; Aurbach, D. Promise and Reality of Post-Lithium-Ion Batteries with High Energy Densities. *Nat. Rev. Mater.* **2016**, *1*, 16013.

(19) Hou, H.; Qiu, X.; Wei, W.; Zhang, Y.; Ji, X. Carbon Anode Materials for Advanced Sodium-Ion Batteries. *Adv. Energy Mater.* **2017**, *7*, 1602898.

(20) Ding, J.; Wang, H.; Li, Z.; Cui, K.; Karpuzov, D.; Tan, X.; Kohandehghan, A.; Mitlin, D. Peanut Shell Hybrid Sodium Ion Capacitor with Extreme Energy−Power Rivals Lithium Ion Capacitors. *Energy Environ. Sci.* **2015**, *8*, 941−955.

(21) Lim, E.; Jo, C.; Kim, M. S.; Kim, M.-H.; Chun, J.; Kim, H.; Park, J.; Roh, K. C.; Kang, K.; Yoon, S.; Lee, J. High Perfomance SodiumIon Hybrid Supercapacitor Based on Nb_2O_5@Carbon Core−Shell Nanoparticles and Reduced Graphene Oxide Nanocomposites. *Adv. Funct. Mater.* **2016**, *26*, 3711−3719.

(22) Chao, D.; Zhu, C.; Yang, P.; Xia, X.; Liu, J.; Wang, J.; Fan, X.; Savilov, S. V.; Lin, J.; Fan, H. J.; Shen, Z. X. Array of Nanosheets Render Ultrafast and High-Capacity Na-ion Storage by Tunable Pseudocapacitance. *Nat. Commun.* **2016**, *7*, 12122.

(23) Sun, J.; Lee, H.-W.; Pasta, M.; Yuan, H.; Zheng, G.; Sun, Y.; Li, Y.; Cui, Y. A Phosphorene−Graphene Hybrid Material as a High-Capacity Anode for Sodium-Ion Batteries. *Nat. Nanotechnol.* **2015**, *10*, 980−985.

(24) Liu, Y.; Zhang, N.; Jiao, L.; Tao, Z.; Chen, J. Ultrasmall Sn Nanoparticles Embedded in Carbon as High Performance Anode for Sodium-Ion Batteries. *Adv. Funct. Mater.* **2015**, *25*, 214−220.

(25) Kim, M. S.; Lim, E.; Kim, S.; Jo, C.; Chun, J.; Lee, J. General Synthesis of N-doped Macroporous Graphene Encapsulated Mesoporous Metal Oxides and Their Application as New Anode Materials for Sodium-Ion Hybrid Supercapacitors. *Adv. Funct. Mater.* **2017**, *27*, 1603921.

(26) Wang, X.; Shen, X.; Wang, Z.; Yu, R.; Chen, L. Atomic-Scale Clarification of Structural Transition of MoS_2 upon Sodium Intercalation. *ACS Nano* **2014**, *8*, 11394−11400.

(27) Park, J.; Kim, J.-S.; Park, J.-W.; Nam, T.-H.; Kim, K.-W.; Ahn, J.-H.; Wang, G.; Ahn, H.-J. Discharge Mechanism of MoS_2 for Sodium Ion Battery: Electrochemical Measurements and Characterization. *Electrochim. Acta* **2013**, *92*, 427−432.

(28) Shi, Z.-T.; Kang, W.; Xu, J.; Sun, Y.-W.; Jiang, M.; Ng, T.-W.; Xue, H.-T.; Yu, D. Y. W.; Zhang, W; Lee, C.-S. Hierarchical Nanotubes

DOI: 10.1021/acsami.7b09813
ACS Appl. Mater. Interfaces 2017, 9, 32745−32755

Assembled from MoS_2-Carbon Monolayer Sandwiched Superstructure Nanosheets for High-Performance Sodium Ion Batteries. *Nano Energy* **2016**, *22*, 27−37.
(29) Cook, J. B.; Kim, H.-S.; Yan, Y.; Ko, J. S.; Robbennolt, S.; Dunn, B.; Tolbert, S. H. Mesoporous MoS_2 as a Transition Metal Dichalcogenide Exhibiting Pseudocapacitive Li and Na-Ion Charge Storage. *Adv. Energy Mater.* **2016**, *6*, 1501937.
(30) Li, Y.; Liang, Y.; Hernandez, F. C. R.; Yoo, H. D.; An, Q.; Yao, Y. Enhancing Sodium-Ion Battery Performance with Interlayer-Expanded MoS_2−PEO Nanocomposites. *Nano Energy* **2015**, *15*, 453−461.
(31) Ding, Y.-L.; Kopold, P.; Hahn, K.; van Aken, P. A.; Maier, J.; Yu, Y. A Lamellar Hybrid Assembled from Metal Disulfde Nanowall Arrays Anchored on a Carbon Layer: In Situ Hybridization and Improved Sodium Storage. *Adv. Mater.* **2016**, *28*, 7774−7782.
(32) Deng, Z.; Jiang, H.; Hu, Y.; Liu, Y.; Zhang, L.; Liu, H.; Li, C. 3D ordered Macroporous MoS_2@C Nanostructure for Flexible Li-ion Batteries. *Adv. Mater.* **2017**, *29*, 1603020.
(33) Xu, J.; Zhang, J.; Zhang, W.; Lee, C.-S. Interlayer Nanoarchitectonics of Two-Dimensional Transition-Metal Dichalcogenides Nanosheets for Energy Storage and Conversion Applications. *Adv. Energy Mater.* **2017**, *7*, 1700571.
(34) Choi, S. H.; Ko, Y. N.; Lee, J.-K.; Kang, Y. C. 3D MoS_2−Graphene Microspheres Consisting of Multiple Nanospheres with Superior Sodium Ion Storage Properties. *Adv. Funct. Mater.* **2015**, *25*, 1780−1788.
(35) Shan, T.-T.; Xin, S.; You, Y.; Cong, H.-P.; Yu, S.-H.; Manthiram, A. Combining Nitrogen-Doped Graphene Sheets and MoS_2: A Unique Film−Foam−Film Structure for Enhanced Lithium Storage. *Angew. Chem., Int. Ed.* **2016**, *55*, 12783−12788.
(36) Kong, D.; He, H.; Song, Q.; Wang, B.; Lv, W.; Yang, Q.-H.; Zhi, L. Rational Design of MoS_2@Graphene Nanocables: Towards High Performance Electrode Materials for Lithium Ion Batteries. *Energy Environ. Sci.* **2014**, *7*, 3320−3325.
(37) Chang, K.; Chen, W.; Ma, L.; Li, H.; Li, H.; Huang, F.; Xu, Z.; Zhang, Q.; Lee, J.-Y. Graphene-Like MoS_2/Amorphous Carbon Composites with High capacity and Excellent Stability as Anode Materials for Lithium Ion Batteries. *J. Mater. Chem.* **2011**, *21*, 6251−6257.
(38) Ye, J.; Chen, W.; Chen, Q.; Yu, Z.; Lee, J. Y. Poly(Diallyldimethylammonium Chloride)-Assisted Synthesis of MoS_2/graphene Composites with Enhanced Electrochemical Performances for Reversible Lithium Storage. *Electrochim. Acta* **2016**, *190*, 538−547.
(39) Wang, X.; Li, G.; Seo, M. H.; Hassan, F. M.; Hoque, M. A.; Chen, Z. Sulfur Atoms Bridging Few-Layered MoS_2 with S-doped Graphene Enable Highly Robust Anode for Lithium-ion Batteries. *Adv. Energy Mater.* **2015**, *5*, 1501106.
(40) Jiang, H.; Ren, D.; Wang, H.; Hu, Y.; Guo, S.; Yuan, H.; Hu, P.; Zhang, L.; Li, C. 2D Monolayer MoS_2−Carbon Interoverlapped Superstructure: Engineering Ideal Atomic Interface for Lithium Ion Storage. *Adv. Mater.* **2015**, *27*, 3687−3695.
(41) Vinayan, B. P.; Nagar, R.; Raman, V.; Rajalakshmi, N.; Dhathathreyan, K. S.; Ramaprabhu, S. Synthesis of Graphene-Multiwalled Carbon Nanotubes Hybrid Nanostructure by Strengthened Electrostatic Interaction and Its Lithium Ion Battery Application. *J. Mater. Chem.* **2012**, *22*, 9949−9956.
(42) Lee, C.; Yan, H.; Brus, L. E.; Heinz, T. F.; Hone, J.; Ryu, S. Anomalous Lattice Vibrations of Single and Few-Layer MoS_2. *ACS Nano* **2010**, *4*, 2695−2700.
(43) Li, H.; Zhang, Q.; Yap, C. C. R.; Tay, B. K.; Edwin, T. H. T.; Olivier, A.; Baillargeat, D. From Bulk to Monolayer MoS_2: Evolution of Raman Scattering. *Adv. Funct. Mater.* **2012**, *22*, 1385−1390.
(44) Brezesinski, T.; Wang, J.; Tolbert, S. H.; Dunn, B. Ordered Mesoporous α-MoO_3 with Iso-Oriented Nanocrystalline Walls for Thin-Film Pseudocapacitors. *Nat. Mater.* **2010**, *9*, 146−151.
(45) Augustyn, V.; Come, J.; Lowe, M. A.; Kim, J. W.; Taberna, P.-L.; Tolbert, S. H.; Abruña, H. D.; Simon, P.; Dunn, B. High-Rate Electrochemical Energy Storage Through Li^+ Intercalation Pseudocapacitance. *Nat. Mater.* **2013**, *12*, 518−522.
(46) Chen, C.; Wen, Y.; Hu, X.; Ji, X.; Yan, M.; Mai, L.; Hu, P.; Shan, B.; Huang, Y. Na^+ Intercalation Pseudocapacitance in Graphene-Coupled Titanium Oxide Enabling Ultra-Fast Sodium Storage and Long-Term Cycling. *Nat. Commun.* **2015**, *6*, 6929.
(47) Le, Z.; Liu, F.; Nie, P.; Li, X.; Liu, X.; Bian, Z.; Chen, G.; Wu, H. B.; Lu, Y. Pseudocapacitive Sodium Storage in Mesoporous Single-Crystal-Like TiO_2−Graphene Nanocomposite Enables High-Performance Sodium-Ion Capacitors. *ACS Nano* **2017**, *11*, 2952−2960.
(48) Hu, Z.; Wang, L.; Zhang, K.; Wang, J.; Cheng, F.; Tao, Z.; Chen, J. MoS_2 Nanoflowers with Expanded Interlayers as High-Performance Anode for Sodium-Ion Batteries. *Angew. Chem., Int. Ed.* **2014**, *53*, 12794−12798.
(49) Wang, X.; Kajiyama, S.; Iinuma, H.; Hosono, E.; Oro, S.; Moriguchi, I.; Okubo, M.; Yamada, A. Pseudocapacitance of MXene Nanosheets for High-Power Sodium-Ion Hybrid Capacitors. *Nat. Commun.* **2015**, *6*, 6544.
(50) Ponrouch, A.; Goñi, A. R.; Rosa Palacín, M. High Capacity Hard Carbon Anodes for Sodium Ion Batteries in Additive Free Electrolyte. *Electrochem. Commun.* **2013**, *27*, 85−88.
(51) Wen, Y.; He, K.; Zhu, Y.; Han, F.; Xu, Y.; Matsuda, I.; Ishii, Y.; Cumings, J.; Wang, C. Expanded Graphite as Superior Anode for Sodium-Ion Batteries. *Nat. Commun.* **2014**, *5*, 4033.
(52) Rudola, A.; Saravanan, K.; Mason, C. W.; Balaya, P. $Na_2Ti_3O_7$: An Intercalation Based Anode for Sodium-Ion Battery Applications. *J. Mater. Chem. A* **2013**, *1*, 2653−2662.
(53) Wang, Y.; Yu, X.; Xu, S.; Bai, J.; Xiao, R.; Hu, Y.-S.; Li, H.; Yang, X.-Q.; Chen, L.; Huang, X. A Zero-Strain Layered Metal Oxide as the Negative Electrode for Long-Life Sodium-Ion Batteries. *Nat. Commun.* **2013**, *4*, 2365.
(54) Xu, Y.; Zhu, Y.; Liu, Y.; Wang, C. Electrochemical Performance of Porous Carbon/Tin Composite Anodes for Sodium-Ion and Lithium-Ion Batteries. *Adv. Energy Mater.* **2013**, *3*, 128−133.
(55) Wang, R.; Lang, J.; Zhang, P.; Lin, Z.; Yan, X. Fast and Large Lithium Storage in 3D Porous VN Nanowires−Graphene Composite as a Superior Anode Toward High-Performance Hybrid Supercapacitors. *Adv. Funct. Mater.* **2015**, *25*, 2270−2278.
(56) Hu, Y.; Luo, B.; Ye, D.; Zhu, X.; Lyu, M.; Wang, L. An Innovative Freeze-Dried Reduced Graphene Oxide Supported SnS_2 Cathode Active Material for Aluminum-Ion Batteries. *Adv. Mater.* **2017**, *29*, 1606132.
(57) Wang, R.; Wang, S.; Jin, D.; Zhang, Y.; Cai, Y.; Ma, J.; Zhang, L. Engineering Layer Structure of MoS_2-Graphene Composites with Robust and Fast Lithium Storage for High-Performance Li-ion Capacitors. *Energy Storage Mater.* **2017**, *9*, 195−205.
(58) Won, J. H.; Jeong, H. M.; Kang, J. K. Synthesis of Nitrogen-Rich Nanotubes with Internal Compartments Having Open Mesoporous Channels and Utilization to Hybrid Full-Cell Capacitors Enabling High Energy and Power Densities Over Robust Cycle Life. *Adv. Energy Mater.* **2017**, *7*, 1601355.
(59) Wang, F.; Wang, X.; Chang, Z.; Wu, X.; Liu, X.; Fu, L.; Zhu, Y.; Wu, Y.; Huang, W. A Quasi-Solid-State Sodium-Ion Capacitor with High Energy Density. *Adv. Mater.* **2015**, *27*, 6962−6968.
(60) Chen, Z.; Augustyn, V.; Jia, X.; Xiao, Q.; Dunn, B.; Lu, Y. High-Performance Sodium-Ion Pseudocapacitors Based on Hierarchically Porous Nanowire Composites. *ACS Nano* **2012**, *6*, 4319−4327.
(61) Liu, S.; Cai, Z.; Zhou, J.; Pan, A.; Liang, S. Nitrogen-Doped TiO_2 Nanospheres for Advanced Sodium-ion Battery and Sodium-Ion Capacitor Applications. *J. Mater. Chem. A* **2016**, *4*, 18278−18283.
(62) Jian, Z.; Raju, V.; Li, Z.; Xing, Z.; Hu, Y.-S.; Ji, X. A High-Power Symmetric Na-Ion Pseudocapacitor. *Adv. Funct. Mater.* **2015**, *25*, 5778−5785.
(63) Thangavel, R.; Moorthy, B.; Kim, D. K.; Lee, Y.-S. Pushing the Energy Output and Cyclability of Sodium Hybrid Capacitors at High Power to New Limits. *Adv. Energy Mater.* **2017**, *7*, 1602654.

DOI: 10.1021/acsami.7b09813
ACS Appl. Mater. Interfaces 2017, 9, 32745−32755

Supporting Information

Elucidating the Intercalation Pseudocapacitance Mechanism of MoS_2-Carbon Monolayer Interoverlapped Superstructure: Toward High-Performance Sodium-Ion-Based Hybrid Supercapacitor

Rutao Wang,[†] Shijie Wang,[†] Xiang Peng,[‡] Yabin Zhang,[†] Dongdong Jin,[†] Paul K Chu,[‡] Li Zhang[†]*

[†]Department of Mechanical and Automation Engineering, The Chinese University of Hong Kong, Shatin NT, Hong Kong SAR 999077, P. R. China.

[‡]Department of Physics and Materials Science, City University of Hong Kong, Tat Chee Avenue, Kowloon, Hong Kong SAR 999077, P. R. China

E-mail: lizhang@mae.cuhk.edu.hk

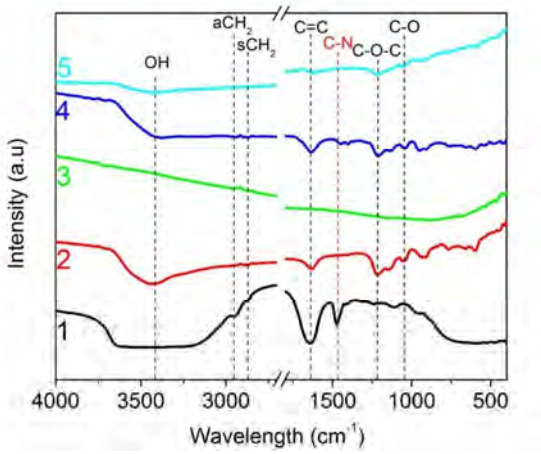

Figure S1. FTIR spectra of as-prepared MoS_2-based samples: 1-PDDA, 2-fresh MoS_2, 3-the annealed MoS_2, 4-MoS_2-PDDA, 5-MoS_2-C.

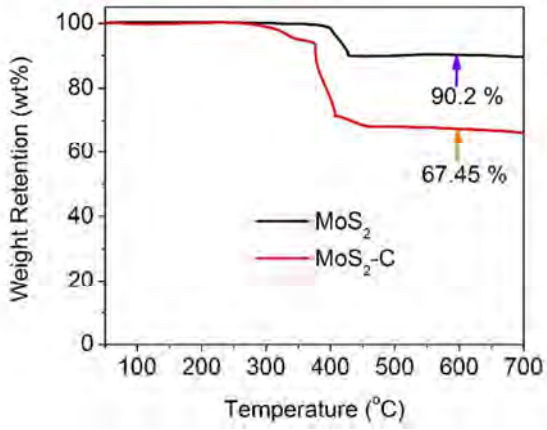

Figure S2. TGA curves of MoS_2 and MoS_2-C samples in air. The weight loss of MoS_2 might be related to the decomposition and oxidation of MoS_2 in air atmosphere. Assuming MoS_2 in MoS_2-C experiences the same weight loss, the content of MoS_2 in MoS_2-C can be calculated as 67.45/90.2=74.77 wt%. The weight retention value in here is obtained at 600 ^{o}C. As we know, the carbon can be completely decomposed at 600 ^{o}C in air. Then the percentage of carbon in MoS_2-C is (100-74.77) wt%=25.23 wt%.

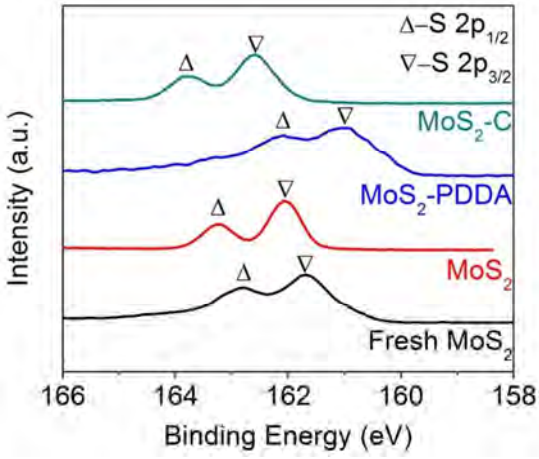

Figure S3. The S 2p core level XPS spectra of the MoS_2 based samples.

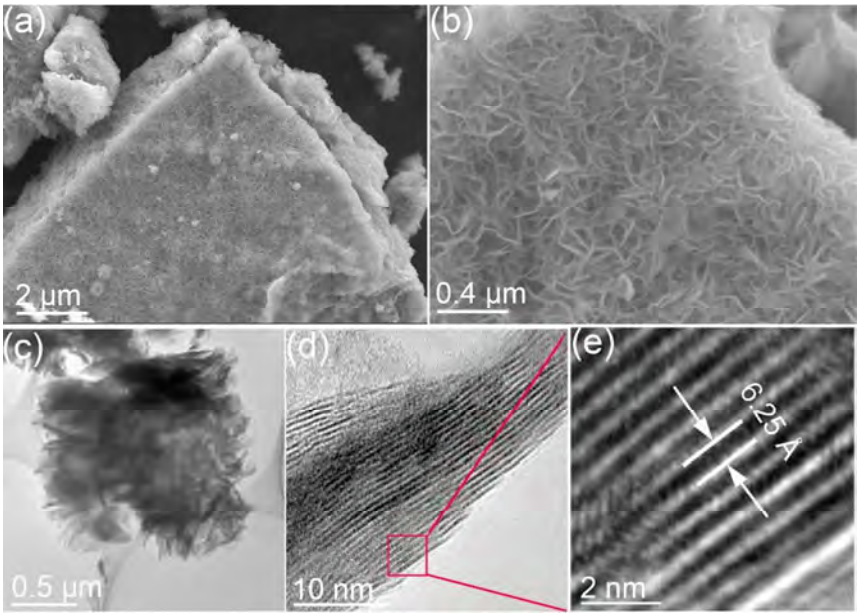

Figure S4. (a) and (b) SEM images, (c) TEM images and (d) and (e) HRTEM images of bare MoS_2 sample.

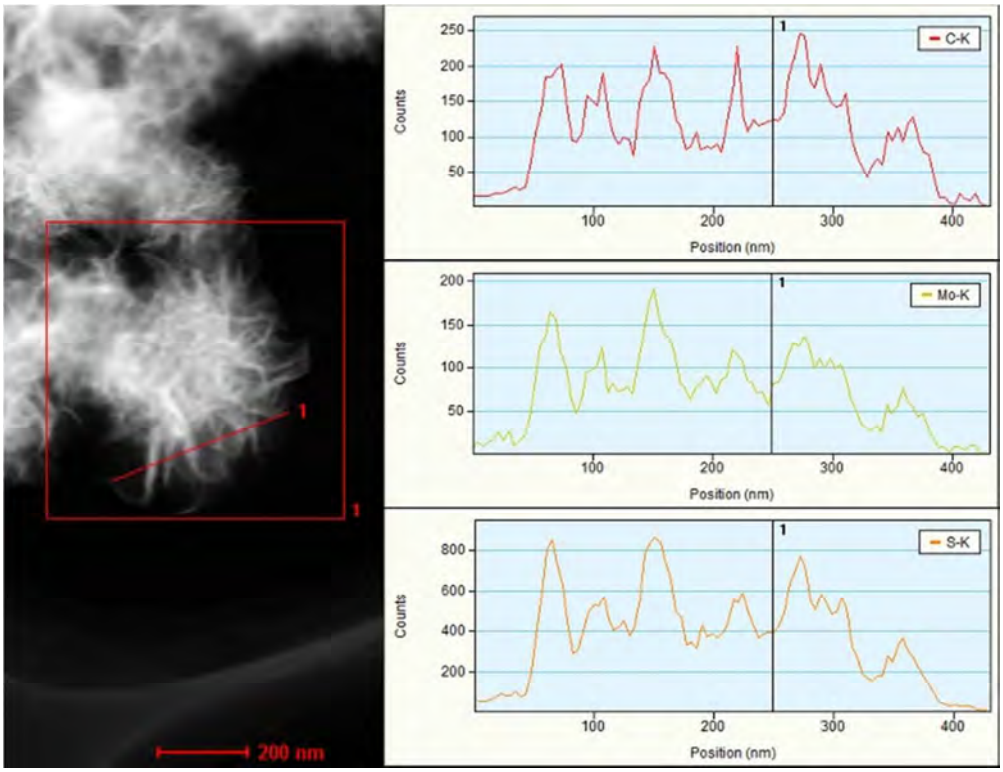

Figure S5. TEM-EDS linear scan profile along the red line in left annual dark-field TEM (ADF-TEM) image of MoS_2-C.

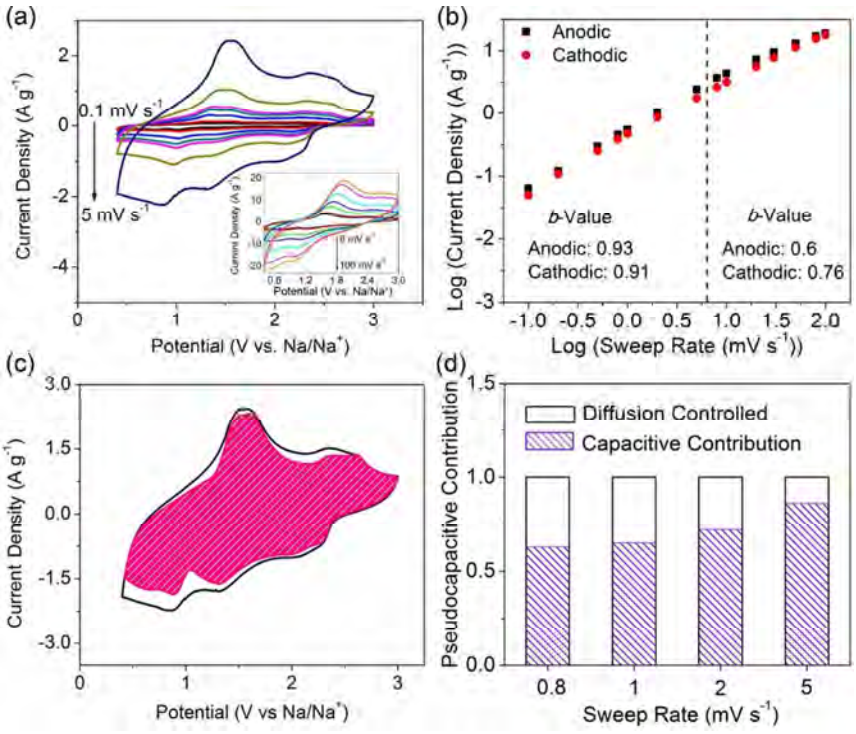

Figure S6. (a) CV curves of MoS_2 at various scan rates for 0.1 to 100 mV s^{-1}. (b) Determination of the *b*-value using the relationship between cathodic peak current and scan rate. (c) Separation of the capacitive and diffusion currents in bare MoS_2 electrode at a scan rate of 5 mV s^{-1}. (d) Contribution ratio of the capacitive charge versus scan rate.

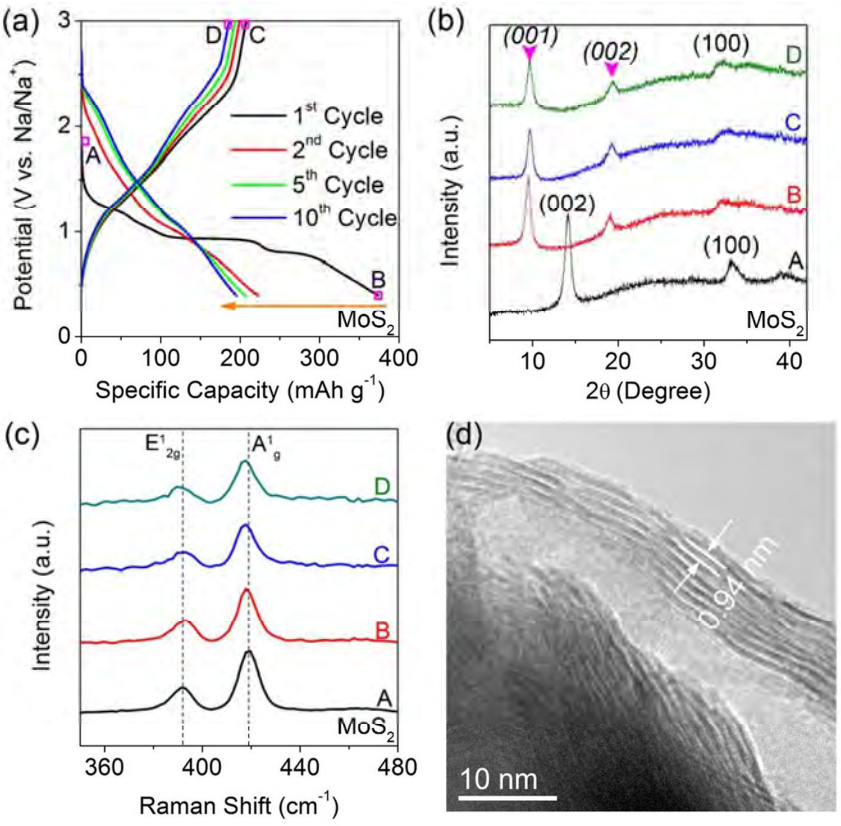

Figure S7. Electrochemical properties and associated structural change of MoS_2. (a) Charge/discharge curves for MoS_2 at a current density of 0.1 A g^{-1}. (b) Ex-situ XRD and (c) Raman patterns of MoS_2 during the different charging/discharging states: pristine state (A), initial sodiated state at 0.4 V (B), initial desodiated state at 3.0 V (C), desodiated state at 3.0 V after 10 cycles (D). (d) HRTEM image of MoS_2 sample during the initial sodiation to 0.4 V.

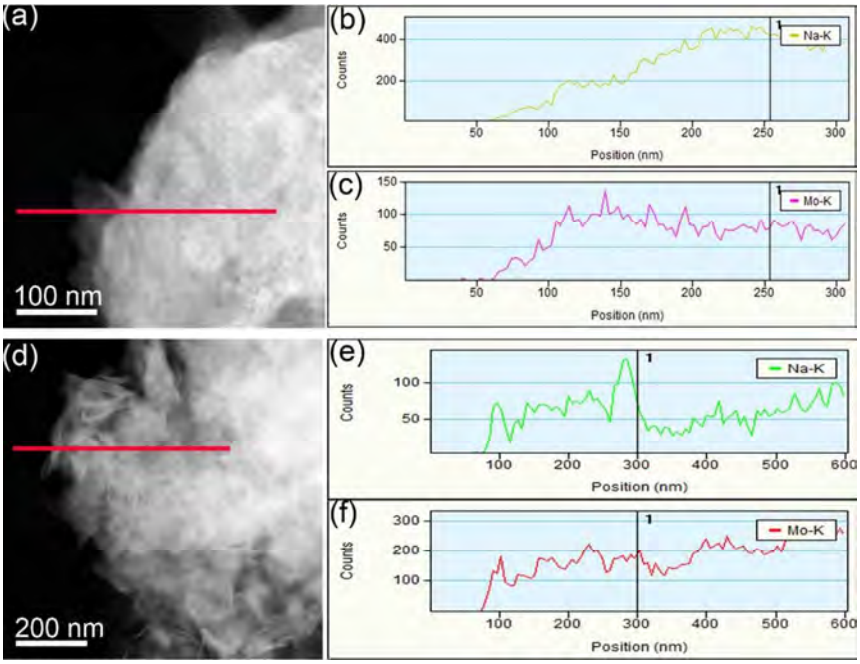

Figure S8. (a) Annular dark-field TEM (ADF-TEM) image of MoS_2 during the initial sodiation to 0.4 V (*vs.* Na/Na^+) and the corresponding linear element mappings detected from red line: (b) Na and (c) Mo. (d) ADF-TEM image of MoS_2 during the initial desodiation to 3.0 V (*vs.* Na/Na^+) and the corresponding linear EDS detected from red line: (e) Na and (f) Mo.

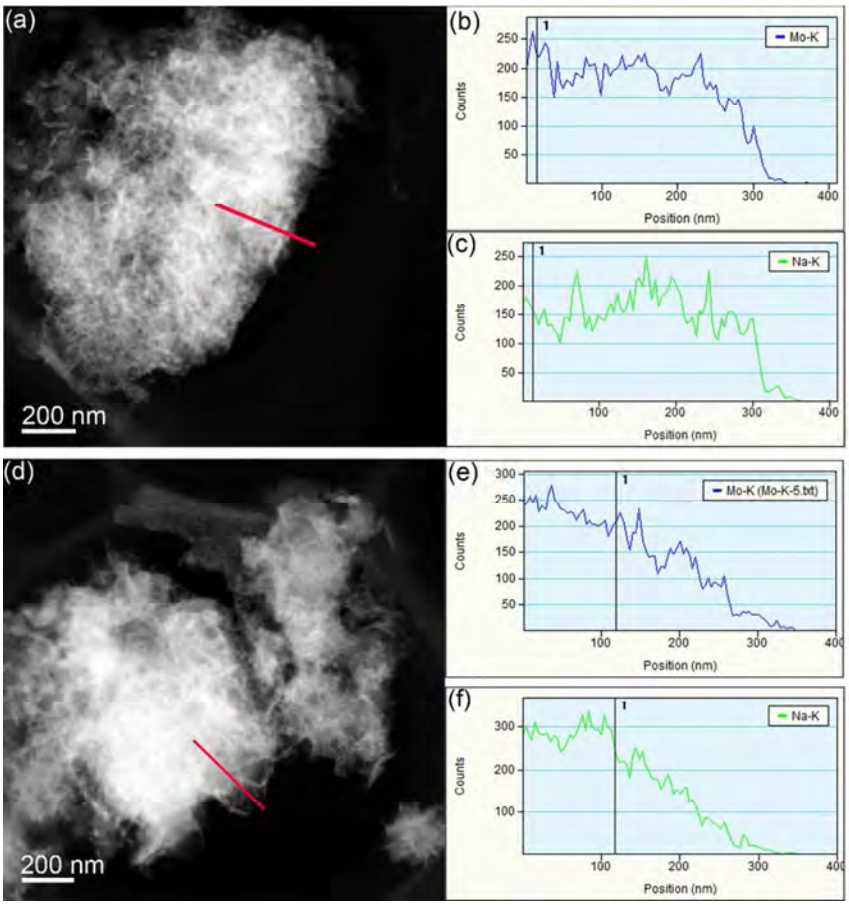

Figure S9. (a) Annular dark-field TEM (ADF-TEM) image of MoS_2-C during the initial sodiation to 0.4 V (*vs.* Na/Na^+) and the corresponding linear element mappings detected from red line: (b) Na and (c) Mo. (d) ADF-TEM image of MoS_2-C during the initial desodiation to 3.0 V (*vs.* Na/Na^+) and the corresponding linear EDS detected from red line: (e) Na and (f) Mo.

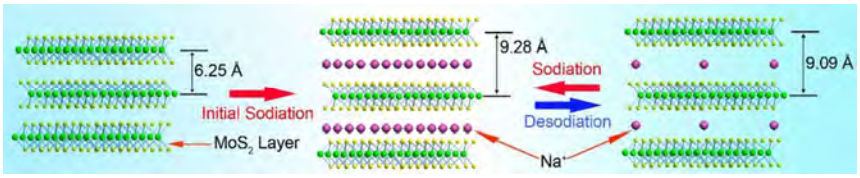

Figure S10. Schematic illustration of the sodium intercalated reaction mechanism of MoS_2.

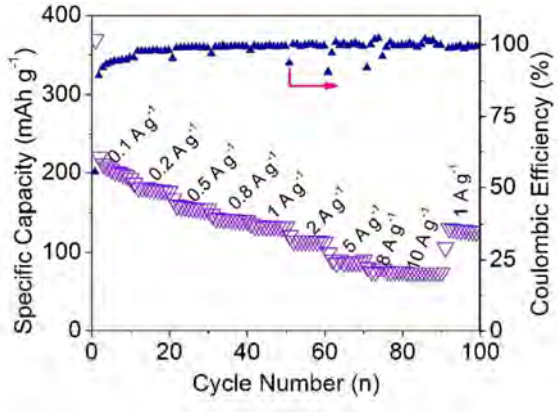

Figure S11. Rate performance for bare MoS_2 electrode at various current density from 0.1 to 10 A g^{-1}.

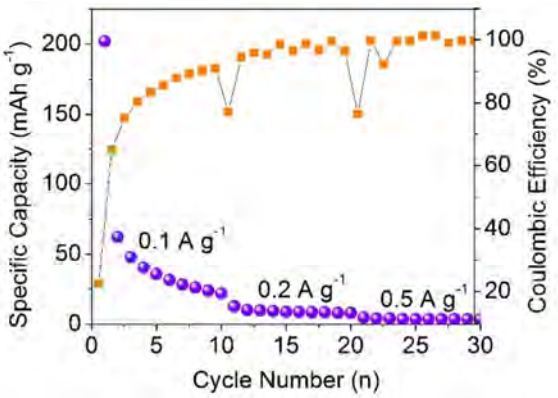

Figure S12. Rate performance for MoS_2-PDDA electrode at various current density from 0.1 to 0.5 A g^{-1}.

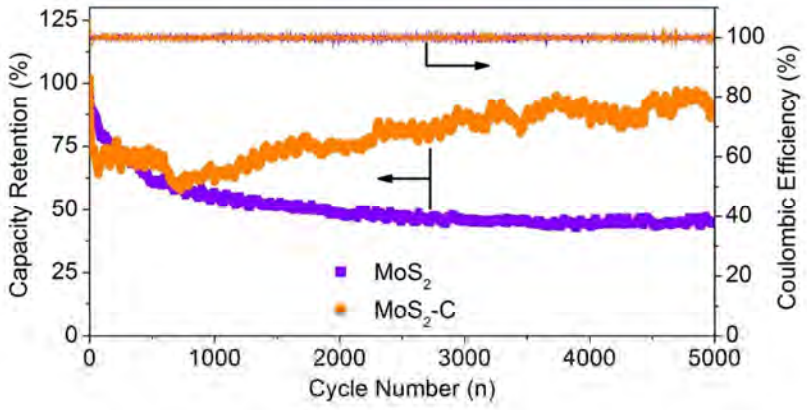

Figure S13. Long-term cycling performances for MoS_2 (purple) and MoS_2-C (orange) at a current density of 5 A g^{-1}

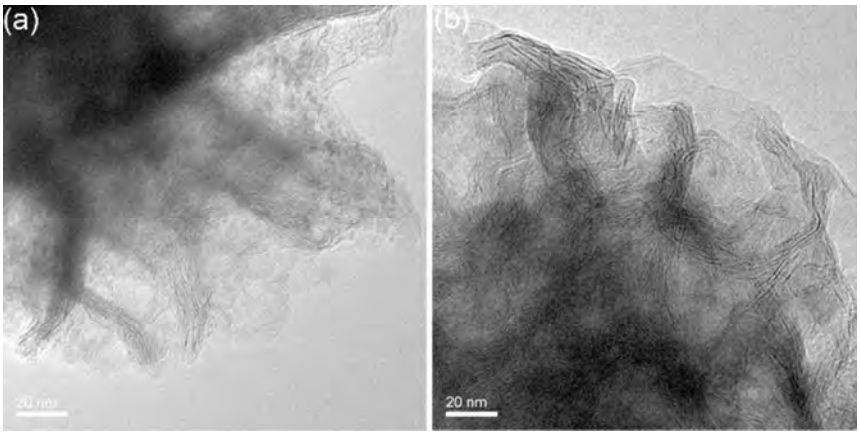

Figure S14. TEM images of MoS_2-C: (a) after 800 cycles at a current density of 1 A g^{-1}, (b) after 5000 cycles at a current density of 5 A g^{-1}.

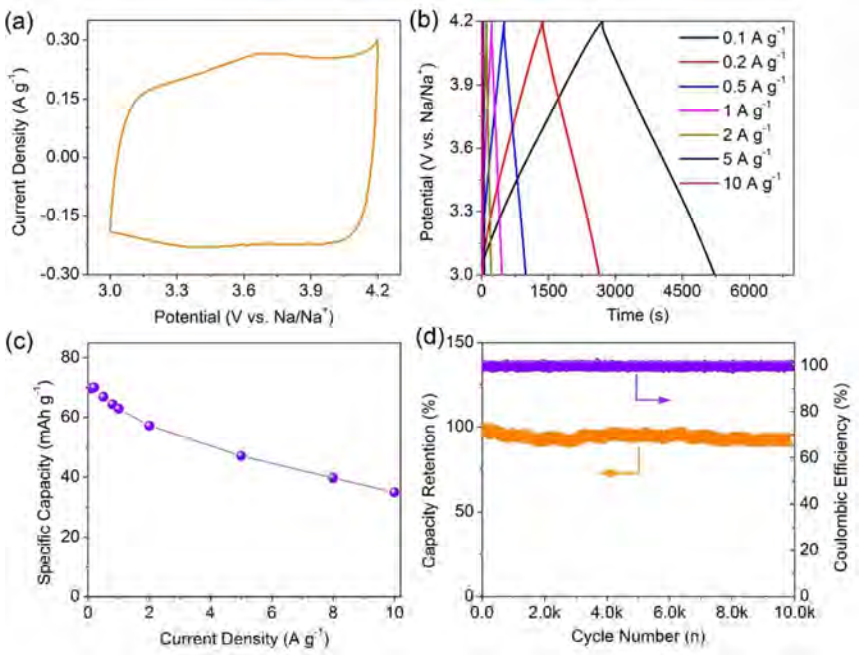

Figure S15. Electrode performance of home-made porous carbon (PDPC) electrode in a half cell. (a) CV curve at 1 mV s^{-1}. (b) Charge/discharge curves at the different current densities from 0.1 to 10 A g^{-1}. (c) Specific capacitance values calculated from galvanostatic charge/discharge curves under different current densities. (d) Cycling stability for 10,000 cycles at a current density of 2 A g^{-1} and the corresponding columbic efficiency of 100%.

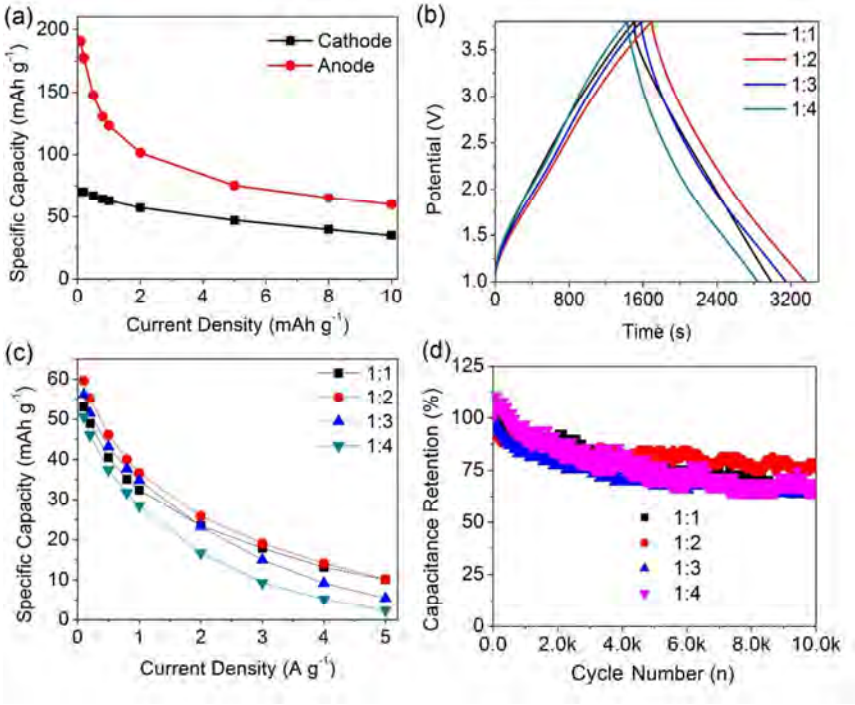

Figure S16. (a) Comparison of specific capacity between cathode and anode active materials. The electrochemical performance of hybrid cell with different anode/cathode mass ratios: (b) galvanostatic charge/discharge curves at different current densities of 0.1 A g^{-1}, (c) specific capacitance values calculated from galvanostatic charge/discharge curves under different current densities, (d) cycling performance of these cell under a current density of 2 A g^{-1}.